2023-05-01

Wave diffraction and radiation from a semi-submersible floating foundation for wind turbine: A semi-analytical study

Zhu, K

10.1063/5.0149411
Physics of Fluids
American Institute of Physics

Title:
Wave diffraction and radiation from a semi-submersible floating foundation for wind turbines: A semi-analytical study

Journal:
Physics of Fluids

Author names and affiliations:
Kai Zhu[1,2], Siming Zheng[2], Simone Michele[2], Feifei Cao[1], Hongda Shi[1,3,4,*], Deborah Greaves[2]

1) Department of Ocean Engineering, College of Engineering, Ocean University of China, Qingdao 266100, China
2) School of Engineering, Computing and Mathematics, University of Plymouth, Drake Circus, Plymouth PL4 8AA, United Kingdom
3) Shandong Provincial Key Laboratory of Ocean Engineering, Ocean University of China, Qingdao 266100, China
4) Qingdao Municipal Key Laboratory of Ocean Renewable Energy, Ocean University of China, Qingdao 266100, China

* Email address for correspondence: hd_shi@ouc.edu.cn

Accepted 2 May 2023

Wave diffraction and radiation from a semi-submersible floating foundation for wind turbines: A semi-analytical study

Kai Zhu (朱凯),[1,2,a)] Siming Zheng (郑思明),[2] Simone Michele,[2] Feifei Cao (曹飞飞),[1] Hongda Shi (史宏达),[1,3,4,b)] and Deborah Greaves[2]

[1)]*Department of Ocean Engineering, College of Engineering, Ocean University of China, Qingdao 266100, China*

[2)]*School of Engineering, Computing and Mathematics, University of Plymouth, Drake Circus, Plymouth PL4 8AA, United Kingdom*

[3)]*Shandong Provincial Key Laboratory of Ocean Engineering, Ocean University of China, Qingdao 266100, China*

[4)]*Qingdao Municipal Key Laboratory of Ocean Renewable Energy, Ocean University of China, Qingdao 266100, China*

Many marine structures are composed of vertical axisymmetric floats. In this paper, a semi-analytical model based on linear potential flow theory and an eigenfunction expansion method is developed to study wave diffraction and radiation by an array of cylindrical structures. Each structure can be formed by three coaxial cylinders of different dimensions. Based on the semi-analytical model, a constrained matrix equation of motion is presented and solved to evaluate the performance of multiple interconnected cylindrical structures. In order to verify the accuracy of the semi-analytical model, a typical OC4-DeepCwind floating offshore wind turbine (FOWT) is selected for validation. The validated model is then applied to study the effect of base column submergence depth, radius and thickness on the motion response of a semi-submersible platform. Although the results of this study are of significance for the selection of the optimum semi-submersible FOWT for specific locations (with specific prevailing wave directions), the focus of this work was placed on the semi-analytical model itself, which is efficient in modelling the interaction of the wave field and can be used in future FOWT projects.

I. INTRODUCTION

Wind energy was anticipated to play a significant and vital part in the energy mix in a carbon-neutral future (UK Department of Energy & Climate Change [1]). In 2020, wind energy was found to be $30\% - 50\%$ cheaper than the UK government's previous estimate made just four years earlier (UK Department for Business, Energy & Industrial Strategy [2]). Consequently, offshore wind turbines are attracting more researchers, engineers, universities, institutes, and governments. Furthermore, offshore wind energy has experienced significant growth due to the stable and strong wind conditions at sea and the availability of larger installation spaces, particularly in deep-sea areas. According to Hong and Möller [3], the mean offshore resources in shallow water at the height of 10 meters are approximately 750 GW, while those in deep water are approximately 1740 GW. Semi-submersible floating offshore wind turbines (FOWT) have leveraged these benefits to emerge as a cost-effective solution for water depths exceeding 50 m, offering the benefits of simple assembly and transportation[4].

In recent years, the development of the semi-submersible FOWT has become a popular research topic, and sophisticated methods are required to evaluate the performance of FOWT systems in light of the fluid-structure interaction (FSI) problem[5]. To date, numerous methods have been employed to investigate the dynamic performance of semi-submersibles, with some methods being utilized extensively. Potential flow theory is one of the most extensively used methods to accurately and efficiently calculate the wave excitation forces on a platform, as well as the added mass and damping due to radiation potential[6]. By transforming hydrodynamic coefficients into the time domain using impulse response functions or state space methods, non-linear problems can be studied[7]. Robertson *et al.* [8], for example, employed the potential flow-based boundary element method (BEM) in the WAMIT software to determine the hydrodynamic coefficients, which are more accurate than those predicted by the Morrison equation. Coulling *et al.* [9] entered the hydrodynamic coefficients into the FAST code and compared various computational results for unstable aerodynamics, hydrodynamics, and fully coupled aerohydrodynamics including mooring line loads with the test date. The results show that FAST accurately captures relevant physics in the coupled floating wind turbine dynamics problem. This method of calculating the hydrodynamic coefficients using potential flow theory and then coupling it with the time-domain code (e.g., FAST, WEC-Sim, etc.) has since become extensively adopted[10].

The solution to hydrodynamic coefficients is critical to the effective application of potential flow theory and serves as the basis for future platform response research. Previously, this problem was typically overcome by the use of commercial softwares or by simplifying the interaction between the floats. For instance, Ghafari et al.[11,12] used a potential flow theory basee on BEM in ANSYS/AQWA software to simulate the DeepCwind semi-submersible floating wind turbines and agreed with available experimental data. The AQWA software was also used to investigate the effect of second-order hydrodynamics on the platform responses of three different semi-submersible platforms in regular waves[13]. These studies demonstrated the efficacy of potential flow theory in solving FSI problems. Furthermore, computational fluid dynam-

[a)]Email: zhukai@stu.ouc.edu.cn

[b)]Author to whom correspondence should be addressed: hd_shi@ouc.edu.cn

ics (CFD) play an important role in this discipline by enabling the direct study of viscous fluids characteristics, albeit at a high computational cost. To account for the viscous effect accurately, Tran and Kim [14] compared CFD results with dynamic motion based on an overset grid and potential-based panel approach for the semi-submersible DeepCWind FOWT. The results show that the CFD results are comparable to the BEM results with viscosity correction. In the process of numerical simulation, model tests are indispensable to verify the accuracy of the numerical simulation results[4,15–20]. For instance, Gou [21] created a 1/50th-scale model of FOWT using Froude scaling at the National Renewable Energy Laboratory (NREL) involving three generic floating platforms: tension-leg platform, a spar-buoy and a semi-submersible. The test results were used to validate, calibrate and potentially improve floating wind turbine design tools such as NREL's aero-hydro-elastic coupling code, FAST[9,10]. However, scaling conflicts between the Froude and the Reynolds numbers are inevitable. Therefore, continuous efforts have been made to improve existing or develop new experimental methods of FOWT[22].

The BEM method, which is based on potential flow theory, has been widely explored, compared, and validated with CFD methodologies and model tests throughout the last decade, confirming its efficiency in studying FSI problems. Furthermore, hydrodynamic coefficients can be employed in time-domain simulations to account for non-linear elements like viscosity, mooring, and wind force, giving a full computational foundation for the total simulation. However, despite their proven speed and accuracy in evaluating the performance of marine structures for several decades, analytical models have yet to be applied for estimating the hydrodynamic coefficients for FOWT.

Although semi-submersible platforms have not been addressed in previous analytical studies, using eigenfunction expansions to solve truncated cylindrical potential functions and Graf's additive formulation to solve multi-body coupling problems provides a profound foundation for this purpose. For instance, Siddorn and Eatock Taylor [23] utilized Yeung's[24] approach of expressing velocity potential as a series of eigenfunctions to solve the diffraction and independent radiation potential of a truncated cylinder array, and Child and Venugopal [25] combined this approach with an algorithm to investigate the configuration of five identically sized truncated cylinders. Zheng and Zhang [26,27] presents an analytical model of the three-dimensional wave diffraction and radiation problem for a truncated cylinder in front of a vertical wall or breakwaters. Recently, a new analytical solution to water wave diffraction and radiation by vertical truncated cylinders in the context of linear potential theory was developed by Li and Liu [28,29], utilizing the multi-term Galerkin method, which is able to model the cube-root singularity of fluid velocity near the edges of the truncated cylinders by expanding the fluid velocity into a set of basis function involving the Gegenbauer polynomials. Due to the study of structures with arbitrary cross-sections can be applied to a wider range of fields, a semi-analytical model of truncated cylinder with a moonpool of arbitrary cross-section is proposed by Zheng *et al.* [30,31]. Additionally, we have divided the waters due to the complex shape of the floating structures, and there are some studies that provide the basis for this, i.e., Ning, Zhou, and Zhang [32] divided the water into six regions to study a novel dual-chamber oscillating water column (OWC) wave energy converter (WEC) based on the linear potential flow theory and eigenfunction expansion technique. Michele *et al.* [33] extended the study of a cylindrical OWC to a hybrid wind-wave energy system and found that the global behavior is strongly influenced by the skirt, while the sloshing eigenfrequencies are impacted by the internal cylinder. The most relevant study to date on FOWT platforms is that of Cong *et al.* [34], who created a theoretical model within the context of linear potential theory to explore the hydrodynamic characteristics of a floating column with a submerged plate attached at the bottom. This structure with a damping plate can be used in various applications, including spar-type platforms and floating wind turbines. However, this study divided the waters into three parts, and radiation potentials and motion responses were not considered.

In this study, the shape of a semi-submersible floating foundation for wind turbines is complex, and the boundary value problem is solved by applying the matching-method of eigenfunctions. Our method entails decomposing the platform into arrays of truncated cylinders of various shapes and then solving for the diffraction and radiation potentials of the mixed flow field within a linearized theory framework to obtain the platform's hydrodynamic coefficients. Each float in our model is formed by three coaxial cylinders, allowing for the radius and draft adjustments to cover the components of semi-submersible platforms (e.g., main columns, base columns, and offset columns of some wind turbine foundations). Practical applications of the model, on the other hand, include a study of the hydrodynamic properties of multiple floating columns with a submerged coaxial plate attached to each column, which allows a plate of any finite thickness to be placed anywhere along the column to investigate the hydrodynamic properties of the damping plate. Based on the semi-analytical model, a constrained matrix equation of motion is provided and solved to evaluate the performance of multiple interconnected cylindrical structures, accounting for both mooring lines and viscous effects on the wind platform. Based on the aforementioned system, the OC4-DeepCwind platform is investigated in this study after running the convergence analysis and model validation. We perform a multiparameter effect analysis, considering the effect of base column submergence depth, radius and thickness on the motion response of the platform.

The rest of this paper is organized as follows. Sec.II presents the governing equations and boundary conditions of wave diffraction and radiation problems. Expressions and solutions to both diffracted potentials and radiated potentials together with wave forces and hydrodynamic coefficients are presented in Sec.III (with algebraic details relegated to the Appendix). The dynamic motion equation is derived in Sec.IV. The semi-analytical model is validated in Sec.V and then used to study the performance of OC4-DeepCwind FOWT in Sec.VI. Conclusions are summarized in Sec.VII.

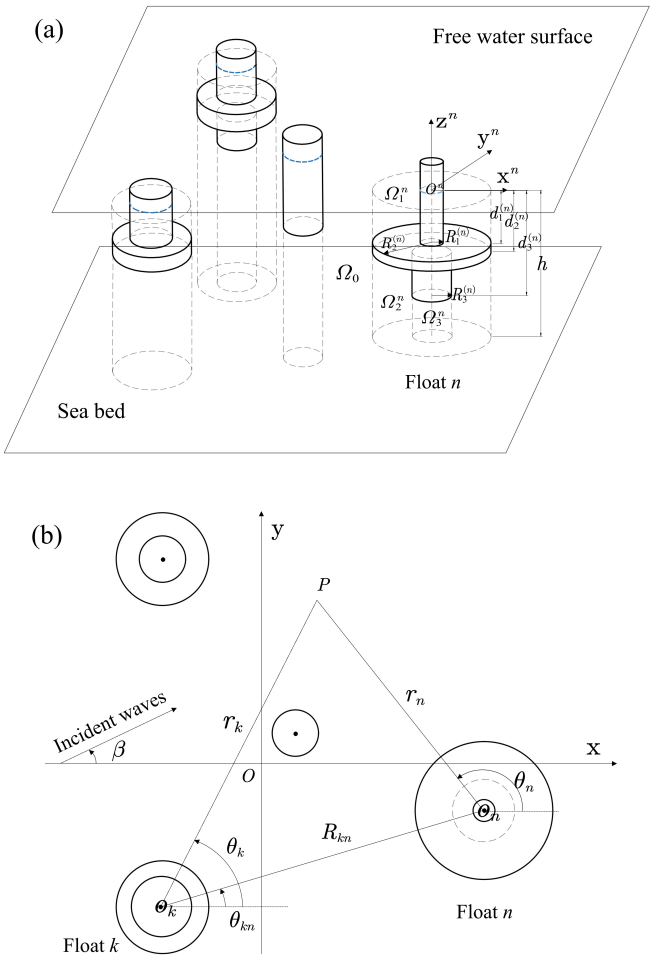

FIG. 1: Definition sketch: (a) bird's-eye view; (b) plan view.

II. MATHEMATICAL MODEL

To study the hydrodynamic characteristics of the marine structure, we consider N cylindrical composite floats, each with different heights and radii, deployed arbitrarily on the free surface of a layer of water with finite depth h and moving independently (see Fig.1a). Each float comprises three parts, namely upper, middle, and bottom parts, with the radii and draft of each part adjusted to ensure that the float shapes cover the components of semi-submersible platforms (e.g., main columns, base columns, and offset columns of wind turbine foundations). The submerged depth and radius of each part are denoted as $d_1^{(n)}$ and $R_1^{(n)}$, $d_2^{(n)}$ and $R_2^{(n)}$, $d_3^{(n)}$ and $R_3^{(n)}$ ($d_3^{(n)} \geq d_2^{(n)} \geq d_1^{(n)}$, $R_2^{(n)} \geq R_1^{(n)}$, $R_2^{(n)} \geq R_3^{(n)}$), respectively.

A general Cartesian coordinate system $Oxyz$ is adopted, with the Oxy plane at the location of the mean water surface and the z-axis pointing upward. The coordinate (point) of the origin and the direction of the x-axis can be arbitrarily specified on the mean water surface. The floats are subjected to a monochromatic incident wave train of small amplitude A and frequency ω propagating at an angle of β relative to the positive x-axis. In addition, for each float, local cylindrical coordinate systems $O_n r_n \theta_n z$ ($n = 1,2,\cdots,N$) are defined (see Fig.1b). The rotation centre of float n is located at ($r_n = 0$, $z = z_n$), which serves as a reference point for calculating the wave excitation forces and hydrodynamic coefficients for the rotary modes. The position of the origin of the float n can be written in terms of the Cartesian coordinate system $Oxyz$ as (x_n, y_n, z_n).

For the analysis, the fluid is divided as follows (see Fig.1a): (a) fluid domains beneath the free water surface and above the middle part, which are denoted as region Ω_1^n (i.e., $R_1^{(n)} \leq r_n \leq R_2^{(n)}, -d_1^{(n)} \leq z \leq 0$); (b) fluid domains beneath the middle part, which are denoted as region Ω_2^n (i.e., $R_3^{(n)} \leq r_n \leq R_2^{(n)}, -h \leq z \leq -d_2^{(n)}$); (c) fluid domains beneath the bottom part, which are denoted as region Ω_3^n (i.e., $0 \leq r_n \leq R_3^{(n)}, -h \leq z \leq -d_3^{(n)}$); (d) remaining fluid domain horizontally extending to infinity, which is denoted as region Ω_0 (i.e., $r_n \geq R_2^{(n)}, -h \leq z \leq 0$ for $n = 1,2,\cdots,N$).

Generally, all floats in the array are free to oscillate independently with six degrees of freedom. We make the usual assumption that the fluid is inviscid, incompressible, and irrotational such that linear theory applies. The total spatial velocity potential ϕ may be decomposed into the incident, diffracted and radiated spatial wave potential as follows:

$$\phi = \phi_I + \phi_D + \sum_{p=1}^{N}\sum_{i=1}^{6} \dot{A}_p^i \phi_{p,i} \tag{1}$$

where ϕ_I is the incident wave potential; ϕ_D is the diffraction potential; $\phi_{p,i}$ is the radiated spatial velocity potential due to unit amplitude velocity oscillation of the float p oscillating in the ith mode (i=1-6, which represents surge, sway, heave, roll, pitch, and yaw, respectively); and $\dot{A}_p^i$ is the complex velocity amplitude of this oscillation.

Following the method in Mei et al.[35], the spatial velocity potential for undisturbed incident waves with amplitude A and frequency ω propagating in the direction β relative to the positive Ox axis may be written as:

$$\phi_I = -\frac{igA}{\omega}\frac{\cosh\left[k_0\left(z+h\right)\right]}{\cosh\left(k_0 h\right)} e^{ik_0(x\cos\beta + y\sin\beta)}, \tag{2a}$$

$$\phi_I(r_n,\theta_n,z) = -\frac{igA}{\omega}\frac{\cosh\left[k_0\left(z+h\right)\right]}{\cosh\left(k_0 h\right)} e^{ik_0\left(\, x_n\cos\beta + y_n\sin\beta\,\right)} \times \sum_{m=-\infty}^{\infty} i^m e^{-im\beta} J_m\left(k_0 r_n\right) e^{im\theta_n}, \tag{2b}$$

where the equation given by Eqs.2a and 2b are in the general Cartesian coordinate system $Oxyz$ and the local cylindrical coordinate system $O_n r_n \theta_n z$, respectively; k_0 denotes the wave number that satisfies the dispersion relation $\omega^2 = g k_0 \tanh\left(k_0 h\right)$; g is the acceleration of gravity; i is the imaginary unit; J_m denotes the Bessel function of the first kind with order m. The free-surface and the body-boundary conditions that ϕ_D and $\phi_{p,i}$ should satisfy are as follows:

Wave diffracted potentials:

$$\frac{\partial \phi_D}{\partial z} = \frac{\omega^2}{g}\phi_D, \quad z = 0 \ \text{ at } \ \Omega_0 \text{ and } \Omega_1^n \ \text{ for } n = 1,2,\cdots,N, \tag{3}$$

$$\frac{\partial \phi_D}{\partial z}=0,\ \ z=-h, \tag{4}$$

$$\frac{\partial \phi_D}{\partial z}=-\frac{\partial \phi_I}{\partial z},\ \ z=-d_j^{(n)}\ \text{ at }\ \Omega_j^n\ \text{ for }\ j=1,2,3, \tag{5}$$

$$\frac{\partial \phi_D}{\partial r_n}=-\frac{\partial \phi_I}{\partial r_n},\ \ -d_j^{(n)}\le z\le -d_{j-1}^{(n)},\ \ r_n=R_j^{(n)}\ \text{ for }\ j=1,2,3, \tag{6}$$

where $d_0^{(n)}=0$.

Wave radiated potentials due to the oscillation of the float p in ith mode:

$$\frac{\partial \phi_{p,i}}{\partial z}=\frac{\omega^2}{g}\phi_{p,i},\ \ z=0\ \text{ at }\ \Omega_0\ \text{ and }\ \Omega_1^n\ \text{ for }\ n=1,2,\cdots,N, \tag{7}$$

$$\frac{\partial \phi_{p,i}}{\partial z}=0,\ \ z=-h, \tag{8}$$

the impermeable condition on the body surface:

$$\frac{\partial \phi_{p,i}}{\partial z}=\begin{cases}0, & i\text{=1,2,6}\\ \delta_{n,p}, & i\text{=3}\\ \delta_{n,p}r_n\sin\theta_n, & i\text{=4}\\ -\delta_{n,p}r_n\cos\theta_n, & i\text{=5}\end{cases},z=-d_j^{(n)}\quad \text{at } \Omega_j^n \text{ for } j=1,2,3, \tag{9}$$

$$\frac{\partial \phi_{p,i}}{\partial r_n}=\begin{cases}\delta_{n,p}\cos\theta_n, & i=1\\ \delta_{n,p}\sin\theta_n, & i=2\\ 0, & i=3,6\ ,\ \ r_n=R_j^{(n)}\\ -\delta_{n,p}(z-z_n)\sin\theta_n, & i=4\\ \delta_{n,p}(z-z_n)\cos\theta_n, & i=5\end{cases},-d_j^{(n)}\le z\le -d_{j-1}^{(n)},\ \text{ for }\ j=1,2,3, \tag{10}$$

where $\delta_{n,p}$ represents the Kronecker delta.

III. THEORETICAL SOLUTION OF DIFFRACTED AND RADIATED POTENTIALS

A. Diffracted/radiated spatial potentials

In different regions, suitable general spatial potentials can be expressed by applying the variable separation method, which involves a complex Fourier series and Bessel functions as follows:

(1) In Region Ω_0

$$\begin{aligned}&\phi_\chi(r_n,\theta_n,z)=\\ &\sum_{m=-\infty}^{\infty}\left\{\frac{A_{m,0}^\chi H_m(k_0r_n)\cosh[k_0(z+h)]}{H_m(k_0R_2^{(n)})\cosh(k_0h)}\right.\\ &\left.+\sum_{j=1}^{\infty}\frac{A_{m,j}^\chi K_m(k_jr_n)\cos[k_j(z+h)]}{K_m(k_jR_2^{(n)})\cos(k_jh)}\right\}e^{im\theta_n}\\ &+\sum_{m=-\infty}^{\infty}\sum_{\substack{k=1\\k\neq n}}^{N}\left\{\left[\frac{A_{m,0}^\chi\cosh[k_0(z+h)]}{H_m(k_0R_2^{(n)})\cosh(k_0h)}\right.\right.\\ &\left.\times\sum_{n'=-\infty}^{\infty}H_{m-n'}(k_0R_{nk})J_{-n'}(k_0r_n)e^{i\left(m\theta_{kn}-n'\theta_{nk}\right)}e^{in'\theta_k}\right]\\ &+\sum_{j=1}^{\infty}\left[\frac{A_{m,j}^\chi\cos[k_j(z+h)]}{K_m(k_jR_2^{(n)})\cos(k_jh)}\right.\\ &\left.\left.\times\sum_{n'=-\infty}^{\infty}K_{m-n'}(k_jR_{nk})I_{-n'}(k_jr_n)e^{i\left(m\theta_{kn}-n'\theta_{nk}\right)}e^{in'\theta_k}\right]\right\}\end{aligned} \tag{11}$$

where $r_k\le R_{nk}$; χ can be either 'D' (for the diffraction potential) or 'p,i' (for the radiated potential); $A_{m,j}^\chi$ are unknown coefficients; H_m is the Hankel function of the first kind of order m; and K_m is the modified Bessel function of the second kind of order m; $I_{-n'}$ is the modified Bessel function of the first kind of order $-n'$.

$$\begin{cases}\omega^2=gk_0\tanh(k_0h), & j=0\\ \omega^2=-gk_j\tan(k_jh), & j\ge 1\end{cases}, \tag{12}$$

(2) In Region Ω_1^n

$$\begin{aligned}&\phi_\chi(r_n,\theta_n,z)=\phi_{S,1}^\chi(r_n,\theta_n,z)+\\ &\sum_{m=-\infty}^{\infty}\left\{\left\{\left[B_{m,0}^\chi\frac{J_m\left(k_0^{(1)}r_n\right)}{J_m\left(k_0^{(1)}R_2^{(n)}\right)}+C_{m,0}^\chi\frac{H_m\left(k_0^{(1)}r_n\right)}{H_m\left(k_0^{(1)}R_2^{(n)}\right)}\right]\right.\right.\\ &\left.\times\frac{\cosh\left(k_0^{(1)}\left(z+d_1^{(n)}\right)\right)}{\cosh\left(k_0^{(1)}d_1^{(n)}\right)}\right\}+\sum_{j=1}^{\infty}\left\{\left[B_{m,j}^\chi\frac{I_m\left(k_j^{(1)}r_n\right)}{I_m\left(k_j^{(1)}R_2^{(n)}\right)}\right.\right.\\ &\left.\left.+C_{m,j}^\chi\frac{K_m\left(k_j^{(1)}r_n\right)}{K_m\left(k_j^{(1)}R_2^{(n)}\right)}\right]\times\frac{\cos\left(k_j^{(1)}\left(z+d_1^{(n)}\right)\right)}{\cos\left(k_j^{(1)}d_1^{(n)}\right)}\right\}\right\}\end{aligned} \tag{13}$$

where

$$\begin{cases}\omega^2=gk_0^{(1)}\tanh\left(k_0^{(1)}d_1^{(n)}\right), & j=0\\ \omega^2=-gk_j^{(1)}\tan\left(k_j^{(1)}d_1^{(n)}\right), & j\ge 1\end{cases}, \tag{14}$$

$B_{m,j}^\chi$ and $C_{m,j}^\chi$ are unknown coefficients; $\phi_{S,1}^\chi$ is a particular solution in Region Ω_1^n, which can be expressed in a coordinate system of the float n for χ = 'D', $\phi_{S,1}^\chi=-\phi_I$; for χ = 'p,i' and $n\neq p$, $\phi_{S,1}^{p,i}(r_n,\theta_n,z)=0$; for $n=p$, $\phi_{S,1}^{n,i}(r_n,\theta_n,z)$ is equal to

$$\phi_{S,1}^{n,i}=\begin{cases}0, & i=1,2,6\\ z+\frac{g}{\omega^2}, & i=3\\ r_n\sin\theta_n\left(z+\frac{g}{\omega^2}\right), & i=4\\ -r_n\cos\theta_n\left(z+\frac{g}{\omega^2}\right), & i=5\end{cases}. \tag{15}$$

(3) In Region Ω_2^n

$$\phi_\chi(r_n,\theta_n,z)=\phi_{S,2}^{\chi}(r_n,\theta_n,z)+ \left[\left[D_{0,0}^{\chi}+E_{0,0}^{\chi}\left(1+\ln\left(\frac{r_n}{R_2^{(n)}}\right)\right)\right]\frac{\sqrt{2}}{2}+ \sum_{j=1}^{\infty}\left[\begin{array}{l} D_{0,j}^{\chi}\dfrac{I_0\left(k_j^{(2)}r_n\right)}{I_0\left(k_j^{(2)}R_2^{(n)}\right)} \\ +E_{0,j}^{\chi}\dfrac{K_0\left(k_j^{(2)}r_n\right)}{K_0\left(k_j^{(2)}R_2^{(n)}\right)}\end{array}\right]\frac{\cos k_j^{(2)}(z+h)}{\cos k_j^{(2)}h}\right], \sum_{\substack{m=-\infty\\ m\neq 0}}^{\infty}\left[\begin{array}{l}\left[D_{m,0}^{\chi}\left(\frac{r_n}{R_2^{(n)}}\right)^{|m|}+E_{m,0}^{\chi}\left(\frac{r_n}{R_2^{(n)}}\right)^{-|m|}\right]\frac{\sqrt{2}}{2} \\ +\sum_{j=1}^{\infty}\left[\begin{array}{l} D_{m,j}^{\chi}\dfrac{I_m\left(k_j^{(2)}r_n\right)}{I_m\left(k_j^{(2)}R_2^{(n)}\right)} \\ +E_{m,j}^{\chi}\dfrac{K_m\left(k_j^{(2)}r_n\right)}{K_m\left(k_j^{(2)}R_2^{(n)}\right)}\end{array}\right]\frac{\cos k_j^{(2)}(z+h)}{\cos k_j^{(2)}h}\end{array}\right]e^{im\theta_n} \tag{16}$$

where

$$k_j^{(2)}=\frac{j\pi}{h-d_2^{(n)}},j=0,1,2,..., \tag{17}$$

$D_{m,j}^{\chi}$ and $E_{m,j}^{\chi}$ are unknown coefficients and $\phi_{S,2}^{\chi}$ is a particular solution in Region Ω_2^n, which is equal to $-\phi_I$ for χ = 'D'; for χ = 'p,i' and $n\neq p$, $\phi_{S,2}^{p,i}(r_n,\theta_n,z)=0$; for $n=p$, $\phi_{S,2}^{n,i}(r_n,\theta_n,z)$ can be expressed in a coordinate system of the float n as

$$\phi_{S,2}^{n,i}=\begin{cases}0, & i=1,2,6\\ \frac{1}{4\left(h-d_2^{(n)}\right)}\left[2(z+h)^2-{r_n}^2\right], & i=3\\ \frac{\sin\theta_n}{8\left(h-d_2^{(n)}\right)}\left[4r_n(z+h)^2-{r_n}^3\right], & i=4\\ \frac{-\cos\theta_n}{8\left(h-d_2^{(n)}\right)}\left[4r_n(z+h)^2-{r_n}^3\right], & i=5\end{cases}. \tag{18}$$

(4) In Region Ω_3^n

$$\phi_\chi(r_n,\theta_n,z)=\phi_{S,3}^{\chi}(r_n,\theta_n,z)+ \times\sum_{m=-\infty}^{\infty}\left[\begin{array}{l} F_{m,0}^{\chi}\left(\frac{r_n}{R_3^{(n)}}\right)^{|m|}\frac{\sqrt{2}}{2} \\ +\sum_{j=1}^{\infty}F_{m,j}^{\chi}\frac{I_m\left(k_j^{(3)}r_n\right)}{I_m\left(k_j^{(3)}R_3^{(n)}\right)}\frac{\cos k_j^{(3)}(z+h)}{\cos k_j^{(3)}h}\end{array}\right]e^{im\theta_n}, \tag{19}$$

where

$$k_j^{(3)}=\frac{j\pi}{h-d_3^{(n)}},j=0,1,2,..., \tag{20}$$

$F_{m,j}^{\chi}$ are unknown coefficients and $\phi_{S,3}^{\chi}$ is a particular solution in Region Ω_3^n, which can be expressed in a coordinate system of the float n for χ = 'D', $\phi_{S,3}^{\chi}=-\phi_I$; for χ = 'p,i' and $n\neq p$, $\phi_{S,3}^{p,i}(r_n,\theta_n,z)=0$; for $n=p$, $\phi_{S,3}^{n,i}(r_n,\theta_n,z)$ is equal to

$$\phi_{S,3}^{n,i}=\begin{cases}0, & i=1,2,6\\ \frac{1}{4\left(h-d_3^{(n)}\right)}\left[2(z+h)^2-{r_n}^2\right], & i=3\\ \frac{\sin\theta_n}{8\left(h-d_3^{(n)}\right)}\left[4r_n(z+h)^2-{r_n}^3\right], & i=4\\ \frac{-\cos\theta_n}{8\left(h-d_3^{(n)}\right)}\left[4r_n(z+h)^2-{r_n}^3\right], & i=5\end{cases}. \tag{21}$$

B. Eigenfunction matching method

The expressions for the diffracted and radiated spatial potentials, as presented in Eqs.(11) - (21) in Sec.III A, satisfy all the boundary conditions given in Eqs.(3) - (10) in Sec.II, except for those at the interfaces of the two adjacent subdomains. The conditions of continuity for the pressure and normal velocity at the boundary can be used to determine the unknown coefficients in Eqs.(11) - (21) for both diffracted and radiated spatial potentials. The continuity conditions for the spatial potentials are as follows:

(1) Continuity of pressure at the boundary $r_n=R_2^{(n)}$:

$$\phi_\chi(r_n^+,\theta_n,z)=\phi_\chi(r_n^-,\theta_n,z),\quad -d_1^{(n)}\le z\le 0 \text{ and } -h\le z\le -d_2^{(n)}, \tag{22}$$

(2) Continuity of pressure at the boundary $r_n=R_3^{(n)}$:

$$\phi_\chi(r_n^+,\theta_n,z)=\phi_\chi(r_n^-,\theta_n,z),\ -h\le z\le -d_3^{(n)}, \tag{23}$$

(3) Continuity of normal velocity at the boundary $r_n=R_1^{(n)}$:

$$\frac{\partial\phi_\chi(r_n^+,\theta_n,z)}{\partial r_n}= \begin{cases} -\frac{\partial\phi_I(r_n^+,\theta_n,z)}{\partial r_n}, & \chi=\text{'}D\text{'}\\ \delta_{n,p}\left[\begin{array}{l}\delta_{1,i}\cos\theta_n+\delta_{2,i}\sin\theta_n\\ -\delta_{4,i}(z-z_n)\sin\theta_n\\ +\delta_{5,i}(z-z_n)\cos\theta_n\end{array}\right], & \chi=\text{'}p,i\text{'}\end{cases}, -d_1^{(n)}\le z\le 0, \tag{24}$$

(4) Continuity of normal velocity at the boundary $r_n=R_2^{(n)}$:

$$\frac{\partial\phi_\chi(r_n^+,\theta_n,z)}{\partial r_n}= \begin{cases} \begin{cases} -\frac{\partial\phi_I(r_n^+,\theta_n,z)}{\partial r_n}, & \chi=\text{'}D\text{'}\\ \delta_{n,p}\left[\begin{array}{l}\delta_{1,i}\cos\theta_n+\delta_{2,i}\sin\theta_n\\ -\delta_{4,i}(z-z_n)\sin\theta_n\\ +\delta_{5,i}(z-z_n)\cos\theta_n\end{array}\right], & \chi=\text{'}p,i\text{'}\end{cases} \text{for } -d_2^{(n)}\le z\le -d_1^{(n)},\\ \frac{\partial\phi_\chi(r_n^-,\theta_n,z)}{\partial r_n}, -d_1^{(n)}\le z\le 0 \text{ and } -h\le z\le -d_2^{(n)}\end{cases}, \tag{25}$$

(5) Continuity of normal velocity at the boundary $r_n=R_3^{(n)}$

$$\frac{\partial\phi_\chi(r_n^+,\theta_n,z)}{\partial r_n}= \begin{cases} \begin{cases} -\frac{\partial\phi_I(r_n^+,\theta_n,z)}{\partial r_n}, & \chi=\text{'}D\text{'}\\ \delta_{n,p}\left[\begin{array}{l}\delta_{1,i}\cos\theta_n+\delta_{2,i}\sin\theta_n\\ -\delta_{4,i}(z-z_n)\sin\theta_n\\ +\delta_{5,i}(z-z_n)\cos\theta_n\end{array}\right], & \chi=\text{'}p,i\text{'}\end{cases} \text{for } -\mathrm{d}_3^{(\mathrm{n})}\le \mathrm{z}\le -\mathrm{d}_2^{(\mathrm{n})}.\\ \frac{\partial\phi_\chi(r_n^-,\theta_n,z)}{\partial r_n}, -h\le z\le -d_3^{(n)}\end{cases}, \tag{26}$$

By substituting the diffracted and radiated spatial potentials from Eqs.(11) - (21) into Eqs.(22) - (26), utilizing the orthogonal properties of the trigonometric function and vertical function, and rearrangements, diffracted spatial potentials and the radiated ones in each subdomain can be obtained by solving a matrix equation[36–38]. The infinite series can be truncated

by selecting $(2M+1)$ terms $(m=-M,...,0,...,M)$ for angular functions and $(J+1)$ terms $(j=0,1,2,...,J)$ for vertical functions. A brief derivation of the calculation of these unknown coefficients is given in Appendix A.

C. Forces and hydrodynamic coefficients

(1) Wave excitation forces and radiation forces

$F_\chi^{n,j}$ represent forces $(j\le 3)$ or moments $(j>3)$ acting on the float n in jth mode. Here, χ = 'D' represents the wave excitation force, and χ = 'p,i' represent radiated force due to unit amplitude velocity oscillation of the float p in ith mode, for which ϕ_I would vanish in the corresponding expressions. The brief derivation and the final complicated formulae for calculating forces and moments are given in Appendix B.

$$F_\chi^{n,j}=\mathrm{i}\omega\rho\sum_{l=1}^{3}\int_{-d_l^{(n)}}^{-d_{l-1}^{(n)}}\int_0^{2\pi}R_l^{(n)}C_j(\phi_I+\phi_\chi)dzd\theta_n,j=1,2, \tag{27}$$

$$F_\chi^{n,j}=\mathrm{i}\omega\rho\int_0^{2\pi}\left[\begin{array}{l}\sum_{l=2}^{3}\int_{R_{l+1}^{(n)}}^{R_l^{(n)}}(\phi_I+\phi_\chi)r_ndr_n\\-\int_{R_1^{(n)}}^{R_2^{(n)}}(\phi_I+\phi_\chi)r_ndr_n\end{array}\right]d\theta_n,j=3, \tag{28}$$

$$F_\chi^{n,j}=\mathrm{i}\omega\rho\times\int_0^{2\pi}\left[\begin{array}{l}\sum_{l=1}^{3}\int_{-d_l^{(n)}}^{-d_{l-1}^{(n)}}R_l^{(n)}C_j(\phi_I+\phi_\chi)(z-z_n)dz\\-D_j\left(\begin{array}{l}\sum_{l=2}^{3}\int_{R_{l+1}^{(n)}}^{R_l^{(n)}}(\phi_I+\phi_\chi)r_ndr_n\\-\int_{R_1^{(n)}}^{R_2^{(n)}}(\phi_I+\phi_\chi)r_ndr_n\end{array}\right)\end{array}\right]d\theta_n,j=4,5, \tag{29}$$

where $R_4^{(n)}=0$,

$$C_j=\left\{\begin{array}{l}-\sin\theta_n,j=2,4\\-\cos\theta_n,j=1,5\end{array}\right.,D_j=\left\{\begin{array}{l}r_n\sin\theta_n,j=4\\r_n\cos\theta_n,j=5\end{array}\right.. \tag{30}$$

(2) Hydrodynamic coefficients

The hydrodynamic coefficients can be written in terms of radiation force asLi and Liu [39]:

$$F_{p,i}^{n,j}=\mathrm{i}\omega a_{p,i}^{n,j}-c_{p,i}^{n,j}, \tag{31}$$

where $a_{p,i}^{n,j}$ and $c_{p,i}^{n,j}$ are added mass and radiation damping of the float n in jth mode due to the float p in ith mode.

IV. EQUATION OF MOTION

This section presents an analytical model for the response of multi-body structures with arbitrary geometric dimensions in regular waves. We consider the n-th interconnected rigid structure floating in the water of constant depth h and subjected to regular waves with small wave amplitude propagating in a direction with an angle β relative to the x-axis of the floats. For such a system, a frequency-domain analysis can be used to efficiently evaluate the floats' dynamics. The dynamic equation of motion for the interconnected floats in the frequency domain is expressed as follows:

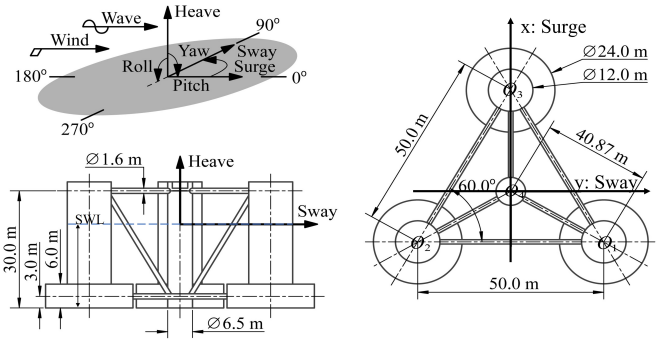

FIG. 2: Coordinate system and dimensions of the OC4-DeepCwind semi-submersible platform[9].

$$\left[\begin{array}{ll}\left[\begin{array}{l}-\omega^2(M_m+M_a)+K_s\\-\mathrm{i}\omega(C_d+C_v)+K_m\end{array}\right] & A_J^T\\A_J & 0\end{array}\right]\left\{\begin{array}{l}X\\F_J\end{array}\right\}=\left\{\begin{array}{l}F\\0\end{array}\right\}, \tag{32}$$

where

$$F=F_e+F_w+F_m, \tag{33}$$

$[F_e]=[F_D^{n,j}]$ is the frequency-dependent complex amplitude of the exciting force array of $(6N\times 1)$ in which N represents the number of structures; X is the complex amplitude of corresponding displacements array of $(6N\times 1)$ for the N structures; M_m is the structure mass matrix of $(6N\times 6N)$; K_s is the hydrostatic restoring matrix of $(6N\times 6N)$; M_a and C_d are the hydrodynamic added mass and damping matrix of $(6N\times 6N)$, respectively; C_v is linearised viscous damping matrix of $(6N\times 6N)$; K_m is the mooring stiffness matrix of $(6N\times 6N)$; wind force F_w acting on the rotor and tower array are both assimilated to a thrust-type force array of $(6N\times 1)$[40]; F_m is the mooring force array of $(6N\times 1)$ due to prestressing[41]; A_J is the displacement constraint matrix of $(N_J\times 6N)$, in which N_J represents the number of rigid constraints; F_J is the rigid force vector of $(N_J\times 1)$, F_e, M_a and C_d can be obtained by solving wave diffraction and radiation problems using the present semi-analytical model.

Here, we take a typical semi-submersible FOWT (OC4-DeepCwind) as an example to study the motion performance, as shown in Fig.2[8,9]. Substituting all the forces acting on the OC4 platform into the Eq.(32), a rigid constraint of four structures for transmitting a force in six degrees of freedom is applied. Specifically, the number of rigid constraints N_J is 18. All elements of the displacement constraint matrix A_J are provided in Appendix C.

V. MODEL VALIDATION

We validate the above-derived theoretical hydrodynamic model for spatial potentials and dynamic motion equation by using a numerical computational fluid dynamics model and published data[13,34]. This includes the validation of wave excitation forces exerting on different floats, hydrodynamic coefficients, and motion response amplitude operator (RAO). The

TABLE I: Main properties of OC4-DeepCwind semi-submersible FOWT.

Designation	Symbol	Value	Unit
Total mass	M_m	14,070,000	kg
Water depth	h	100	m
Wave heading	β	0	rad
Total draft	$d_3^{(n)}$	20	m
Bottom of base column depth	$d_2^{(n)}$	20	m
Top of base column depth	$d, d_1^{(n)}$	14	m
Base column thickness	l	6	m
Spacing between offset columns	S	50	m
Radius of the central column	R_c	3.75	m
Radius of offset column	$R_1^{(n)}$	6	m
Radius of base column	$R, R_2^{(n)}$	12	m

dimensionless quantities of the wave excitation forces and hydrodynamic coefficients are defined as[42,43]:

$$\overline{F}_{\chi}^{n,j} = \frac{\left|F_{\chi}^{n,j}\right|}{\rho g R_0{}^{i'} A}, \tag{34}$$

where R_0 is a reference length, unless otherwise stated, $R_0 = 6$ m is selected for the OC4-DeepCwind semi-submersible platform; $i' = 2$ for $j = 1-3$ and $i' = 3$ for $j = 4-5$.

$$\overline{a}_{p,i}^{n,j} = \frac{a_{p,i}^{n,j}}{\rho R_0^{i'}}; \quad \overline{c}_{p,i}^{n,j} = \frac{c_{p,i}^{n,j}}{\omega \rho R_0^{i'}}, \tag{35}$$

where $i' = 3$ for $(i,j) = (1-3, 1-3)$; $i' = 4$ for $(i,j) = (1-3, 4-5)$ and $(4-5, 1-3)$; whereas $i' = 5$ for $(i,j) = (4-5, 4-5)$.

A conventional BEM-based commercial code (ANSYS AQWA, 2022) is adopted to study the wave diffraction and radiation problem for the OC4-DeepCwind FOWT. The main properties of the OC4-DeepCwind are presented in Table I, where all the parameters are chosen according to the previous studies by Robertson et al.[8] and Zhang et al.[13]. The CPU time required to achieve the numerical simulation using 21910 wetted elements is about 26 mins for each frequency.

We conducted a convergence analysis using Eigen-series analysis to ensure accurate results. In Figs.3 and 4, the convergence study of the wave excitation forces and hydrodynamic coefficients are presented to illustrate the impact of the vertical and angular truncated cut-offs (i.e., in terms of J and M), respectively. In order to obtain the converged results, $J \geq 25$ and $M \geq 3$ are suggested as learnt from Figs.3 and 4. Hereinafter, $J = 30$ and $M = 4$ are adopted. The CPU time required for solving the diffraction and radiation problem for each wave frequency is merely about 83 s by the semi-analytical model, providing a more efficient tool than numerical models. The excellent agreement between the semi-analytical and numerical results verifies the accuracy of the semi-analytical model in solving wave diffraction and radiation problem. Meanwhile, the solutions of the present semi-analytical are compared with Cong et al.[34] and Zhang et al.[13] as follows.

A. Single structure validation

A theoretical model of a compound column-plate structure was developed by Cong et al.[34] to study hydrodynamic characteristics. We used a scaled system, with the same device geometry, sea state, and water depth as Cong et al. (2018, Fig.8)[34], to facilitate better comparison with Cong's previous work, i.e. N= 1, $d_2^{(1)}/R_1^{(1)} = 1$, $l/R_1^{(1)} = 0.1$, $h/R_1^{(1)} = 3$ and $d_2^{(1)} = d_3^{(1)}$. In Fig.5, the present analytical results are consistent with the results of Cong's, indicating that the analytical solution can accurately calculate the wave excitation forces for a single structure.

B. Multiple structures validation

To validate the accuracy of the hydrodynamic coefficients and motion equation Eq.(32) for the multi-body structure, the hydrodynamic coefficients are brought into the motion equation to investigate the motion response of the OC4-DeepCwind semi-submersible FOWT. The same computational parameters as those used in Zhang et al.'s study (2020, Section 4.1, Fig.6)[13] are used here. The excellent agreement between the semi-analytical solutions and Zhang et al.[13] confirms the accuracy of the semi-analytical model in solving the hydrodynamic coefficients and dynamic motion equation for the multi-body structure (see Fig.6).

VI. RESULTS AND DISCUSSION

Submerged plates are often installed on floating structures to improve their seakeeping capability. Although the attached plate provides an additional immersed body surface that receives fluid action and aggravates the wave loads, the effects of added mass and radiation damping can help suppress the motion response. Due to the complexity of the effects of submerged plates on structures, the base column of the OC4 platform is investigated in this section, focusing on the effects of the submergence depth $d_1^{(n)}$, radius $R_2^{(n)}$ and thickness l on the platform motion response. In each case, calculations are performed with the same linear viscous correction and mooring stiffness matrix used in Sec.V (Fig.6) at a water depth of 100 m.

A. Effect of base column submergence depth

The correlation between the motion performance and base column submergence depth $d_1^{(n)}$ is investigated in this subsection. For brevity, we use the generic symbol d instead of $d_1^{(n)}$.

Fig.7 presents the curve of surge motion X_1 as a function of angular frequency ω and base column submergence depth d with R = 12 m and l = 6 m. For a clearer display of the curves, Fig.7b and 7c are detailed views of Fig.7a. As ω increases from 0 rad/s, the response of surge motion significantly decreases when $\omega \leq 0.8$ rad/s, and the decline of X_1 tends to be slower as ω further increases. For any specified value of d, a local peak of X_1 occurs at $0.85 < \omega < 1.15$ rad/s. This peak is sensitive to changes in d (see Fig.7b). In this region, X_1 notably increases with the decrease in d, where the peak value rises from 0.25 to 0.37 as d decreases from 14 to 6 m, reflecting an increase of 48%. The peak further increases with the d decreases from 6 to 3 m, representing an increase of 140%.

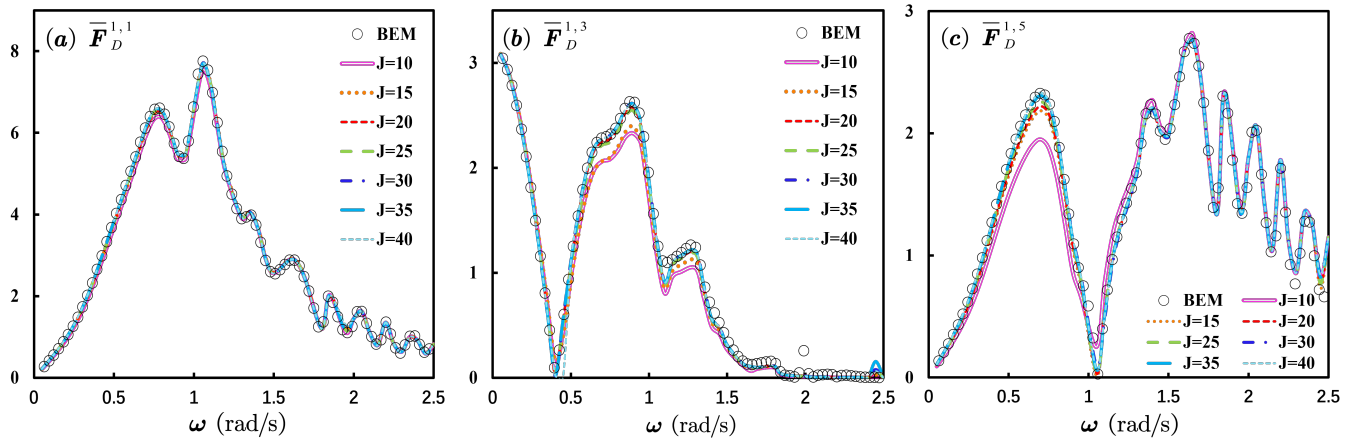

FIG. 3: Impact of the vertical cut-offs (i.e., in terms of J) on wave excitation forces, $M = 5$: (a) $\overline{F}_D^{1,1}$; (b) $\overline{F}_D^{1,3}$; (c) $\overline{F}_D^{1,5}$.

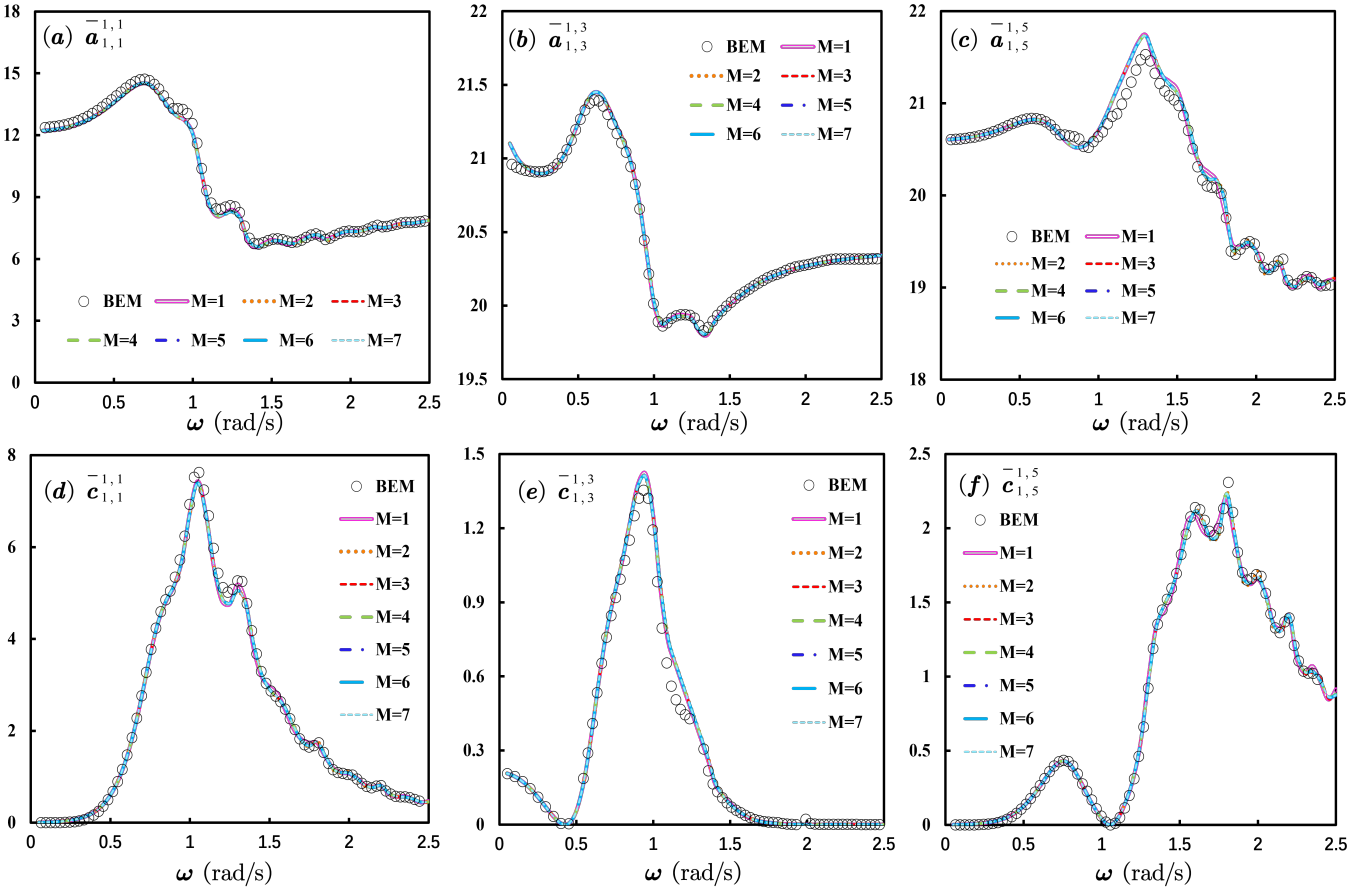

FIG. 4: Impact of the angular cut-offs (i.e., in terms of M) on hydrodynamic coefficients, $J = 30$: (a) $\overline{a}_{1,1}^{1,1}$; (b) $\overline{a}_{1,3}^{1,3}$; (c) $\overline{a}_{1,5}^{1,5}$; (d) $\overline{c}_{1,1}^{1,1}$; (e) $\overline{c}_{1,3}^{1,3}$; (f) $\overline{c}_{1,5}^{1,5}$.

This indicates that the base column at the bottom of the offset column is critical for ensuring the stability of the platform in surge mode. In other words, it is advisable to avoid $d \leq 6$ m at $0.85 < \omega < 1.15$ rad/s. Conversely, for $\omega \geq 1.15$ rad/s, the value of X_1 decreases with increasing d, indicating that the increasing radiation damping and additional mass play dominant roles compared to the wave force.

Fig.8 plots the heave motion X_3 against different values of d and ω. Compared to X_1, X_3 is more sensitive to changes in d, especially at $\omega < 0.42$ rad/s. As shown in Fig.8b, the peak

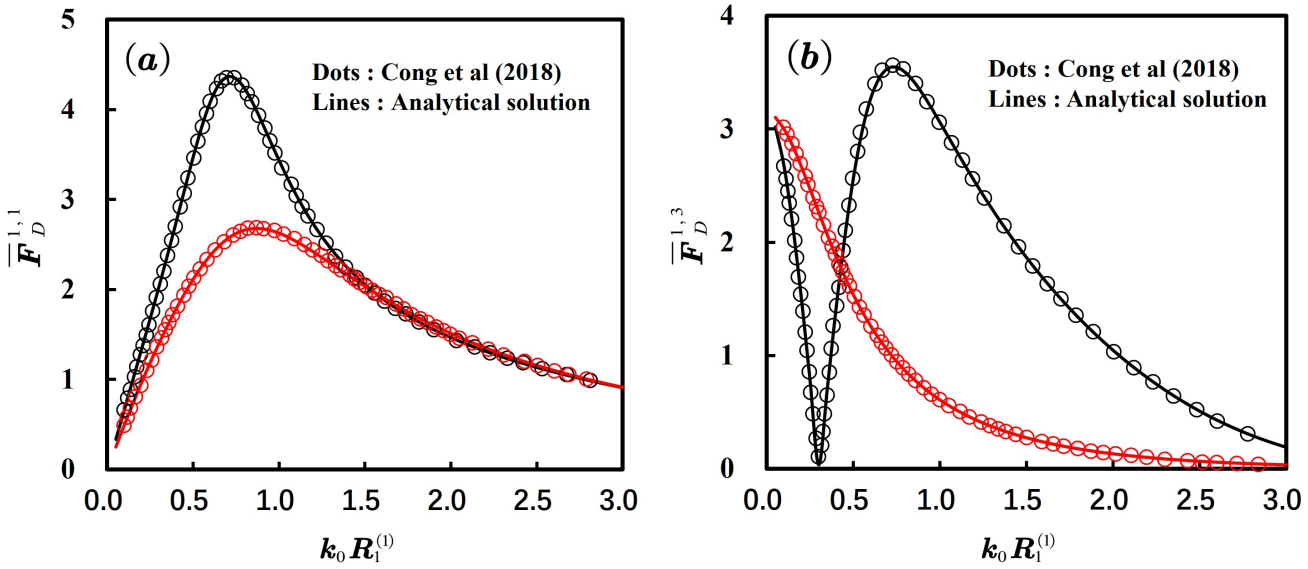

FIG. 5: Comparision normalized linear wave force amplitude (black: $R_2^{(1)}/R_1^{(1)} = 2$, red: $R_2^{(1)}/R_1^{(1)} = 1$): (a) horizontal force; (b) vertical force.

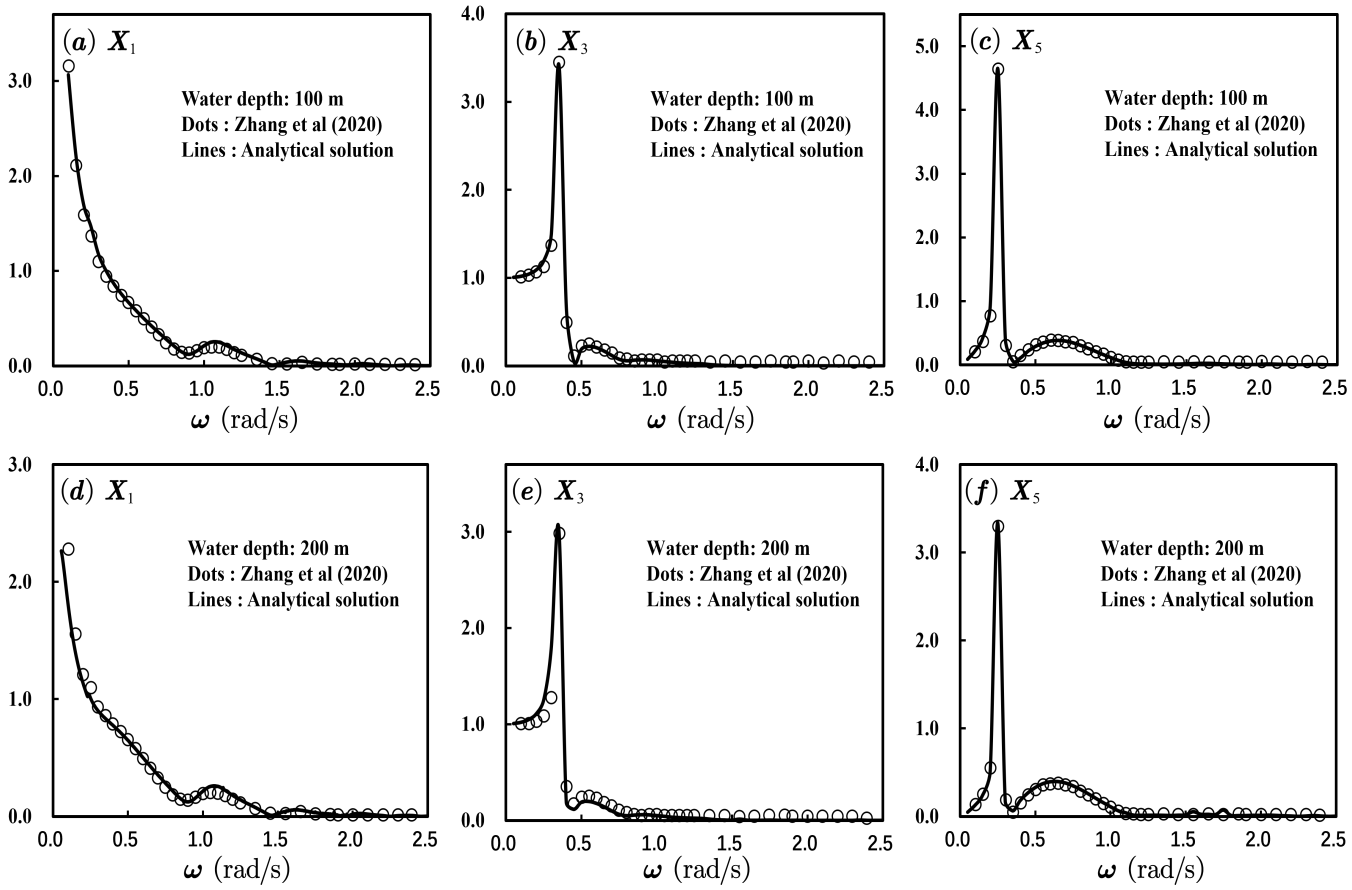

FIG. 6: Comparision RAOs of OC4-DeepCwind semi-submersible FOWT. (a) and (d) Surge RAO (m/m), (b) and (e) Heave RAO (m/m), (c) and (f) Pitch RAO (deg/m); (a)-(c) in 100 m water depth; (d)-(f) in 200 m water depth.

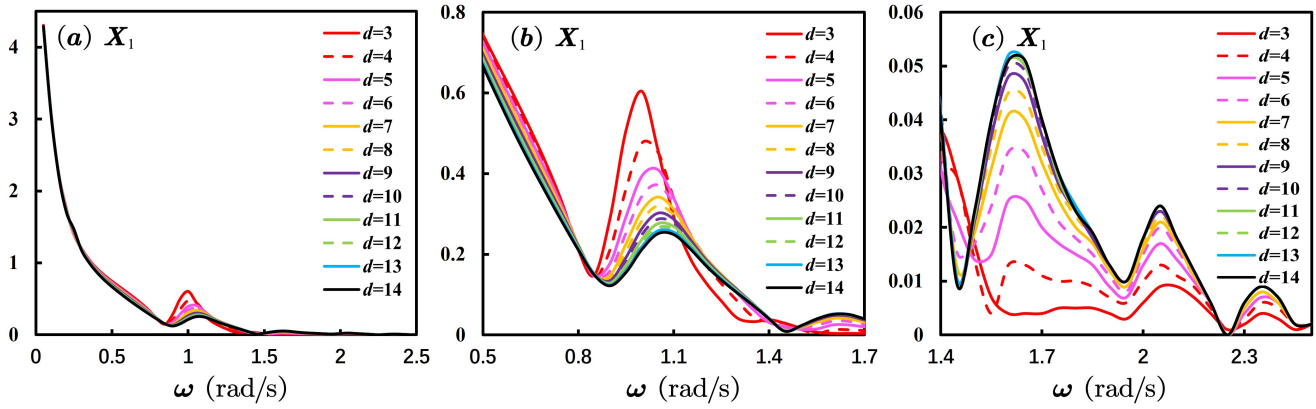

FIG. 7: Variation of the response of the surge mode in terms of the unit amplitude (m/m) with R = 12 m and l = 6 m for different submergence depths; (b) and (c) are detailed descriptions for (a), respectively.

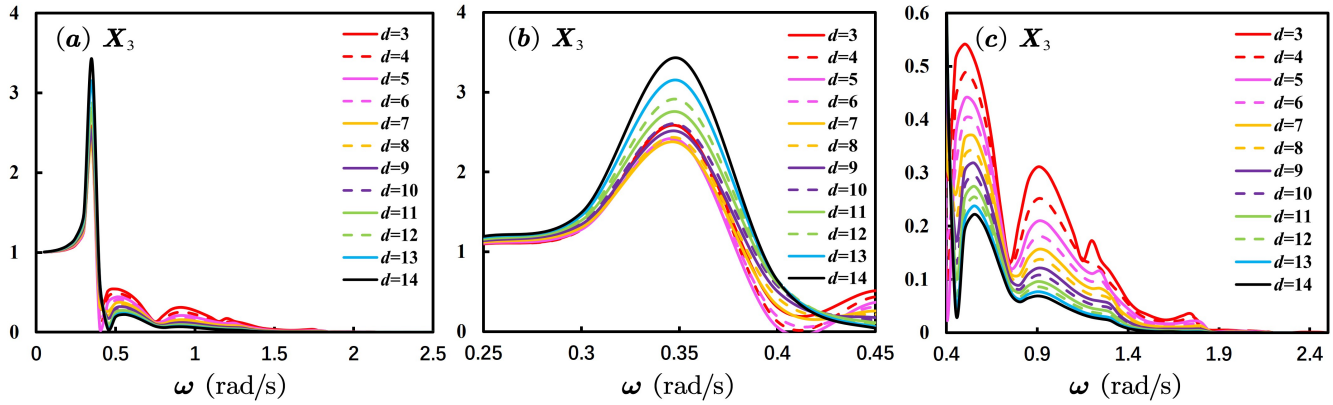

FIG. 8: Variation of the response of the heave mode in terms of the unit amplitude (m/m) with R = 12 m and l = 6 m for different submergence depths; (b) and (c) are detailed descriptions for (a), respectively.

value of X_3 around $\omega = 0.35$ rad/s decreases from 2.57 to 2.39 as d increases from 3 to 5 m. At an optimal d of approximately 5 m, the local peak value at peak frequency is minimized, and X_3 decreases by 43% from d = 14 to 5 m. However, for $\omega \geq 0.42$ rad/s, the trend changes, and X_3 increases monotonically as d decreases. The peaks become more pronounced at two locations: for $d = 14$ m, $X_3 = 0.22$ at $\omega = 0.5$ rad/s and $X_3 = 0.07$ at $\omega = 0.9$ rad/s; for $d = 3$ m, X_3 is 0.54 and 0.31, respectively. As ω keeps increasing, X_3 decreases and stays at a low value for $\omega \geq 1.4$ rad/s.

Fig.9 illustrates the motion response curve for the pitch mode, which exhibits similarities to that of the heave mode. For $\omega < 0.4$ rad/s, the value of X_5 rapidly increases with decreasing d within the range of 8 m $\leq d \leq$ 14 m, while it significantly increases with d within the region of 3 m $\leq d \leq$ 8 m. The maximum and minimum peak values $X_5 = 12.65$ and $X_5 = 4.65$ occur at $\omega = 0.25$ rad/s, $d = 8$ m and $d = 14$ m (see Fig.9b). In the region of $\omega > 0.4$ rad/s, X_5 increases with decreasing d, but the amplitude is small. For any specified value of X_5, two peaks are visible in the $X_5 - \omega$ curve: one is 1.02 occurring around $\omega = 0.75$ rad/s, $d = 3$ m and 0.38 for $d = 14$ m; the other one is 0.33 at $\omega = 1.15$ rad/s, $d = 3$ m and 0.08 for $d = 14$ m. This means that the pitch value of X_5 at $\omega \geq 0.42$ rad/s is smaller than 1.02, indicating that the pitch motion in this region can be ignored.

Based on the overview of the submergence depth effect, the influence of the submergence depth d on the heave and pitch modes is more significant than on the surge mode, and shows distinct regularity of variation in each mode. For 1.4 rad/s $> \omega \geq 0.42$ rad/s, the value of the motion response in each mode decreases with increasing d value. Note that X_1, X_2 and X_3 are less than 0.6, 0.27, and 0.33, respectively, for $\omega \geq 1$ rad/s. In particular, for $\omega \geq 1.4$ rad/s, X_1, X_2 and X_3 are less than 0.05, 0.06, and 0.12, respectively, indicating that the effect of d is negligible. The difference is that, when $\omega < 0.42$ rad/s, the d is slightly influenced in X_1, while in the heave mode, X_3 first decreases and then increases with d and the peak value at $d = 5$ m is 43% smaller than that at $d = 14$ m. In the pitch mode, the trend is the reverse version of that of the heave motion, that is, first increases and then decreases and a 170% increase in the peak value is observed at $d = 8$ m compared with $d = 14$ m. These performances provide the preconditions for the optimisation of d. For example, if the local sea state is dominated by frequencies greater than 0.3 rad/s, an

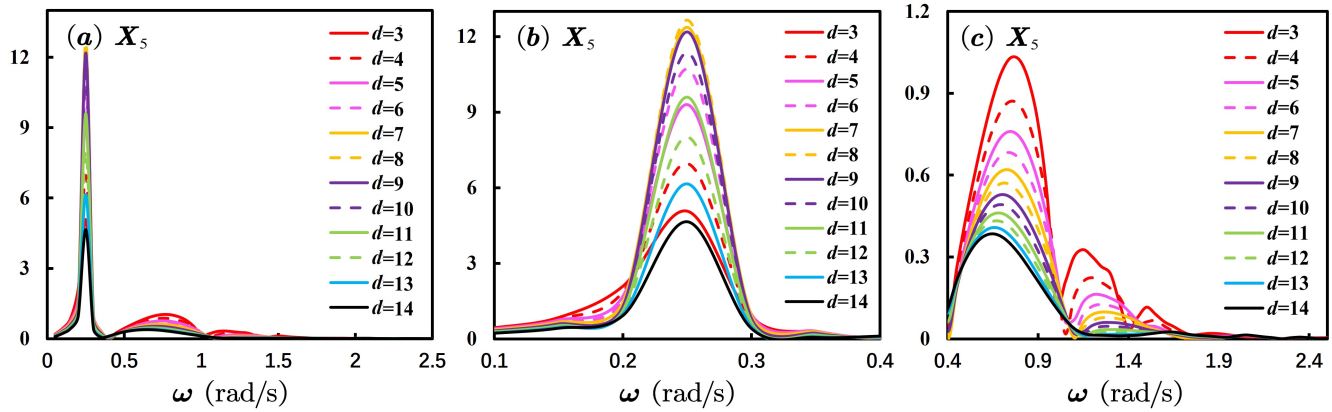

FIG. 9: Variation of the response of the pitch mode in terms of the unit amplitude (deg/m) with R = 12 m and l = 6 m for different submergence depths; (b) and (c) are detailed descriptions for (a), respectively.

appropriate d value should reduce the peak of vertical motion significantly while ensuring that the surge and pitch motions are not too large. For such a condition, $d = 14$, 11, or 10 m may be appropriate, given that the maximum pitching motion occurs in the range of 0.2 to 0.3 rad/s, whereas the maximum vertical motion occurs in the range of 0.3 to 0.4 rad/s. This is important for engineering applications, but multi-parameter optimisation is necessary[44,45] and is briefly analysed here in the frequency domain.

Additionally, the motion response displays multiple peaks and troughs across the entire frequency range, which can be attributed to Bragg resonance, as shown in Figs.7b and 7c[46–48]. When the spacing S_r between successive scatterers is half-integral multiples of the incident wavelength, i.e. $k_0 S_r \cos\beta' = n_B\pi$, where n_B is a positive integer and β' is the angle between the incident wave and the line connecting the centroids of the base columns, constructive interference gives rise to strong reflection[49,50]. In this study, the Bragg resonances are primarily generated by reflections between the offset columns, where the separation distance S_r consists of two parts: the upper part is the distance between the offset columns $S_{r1} = (l - 2R_1^{(n)})\cos\beta'$, and the bottom part is the distance between the base columns $S_{r2} = (l - 2R_2^{(n)})\cos\beta'$. When incident waves propagate along the x-axis, the Bragg resonance position calculated from the separation distance S_{r1} is expected to occur at ω_{r1} =0.97, 1.22, 1.68, 1.93$\cdots$rad/s, while the position calculated from S_{r2} should occur at ω_{r2} =1.36, 1.72, 2.11, 2.43$\cdots$rad/s, based on Bragg's law. To further investigate the Bragg resonance phenomenon, Fig.10 presents the dimensionless quantities of the wave excitation force. It can be observed that the peak frequencies ω_r resulting from the effect of Bragg resonance are 1.25, 1.64, 2.04, 2.37$\cdots$ rad/s, which fall within the range of $\omega_{r1} < \omega_r < \omega_{r2}$. Moreover, ω_r is consistent with the peak frequencies depicted in Figs.7b and 7c.

The Bragg resonance phenomenon is also observed in the heave and pitch modes, as depicted in Figs.8a and 9a. The first peak frequency observed in the $X_3 - \omega$ and $X_5 - \omega$ curves correspond to the eigenfrequency ω_h of the wind turbine platform. This eigenfrequency can be calculated by $\omega_h = \sqrt{s_w/(M_m + m_a)}$, where s_w and m_a denote the platform stiffness and radiation added mass of the platform, respectively. The second peak frequency observed in Figs.8a and 9a are consistent with the main (first) peak frequency of the wave excitation force seen in Fig.10, which is determined by the geometric and mass properties of the structure. In the absence of structure interaction, only this main peak would be observed, such as for a single truncated cylinder in the wave. The remaining peaks are caused by the Bragg resonance phenomenon. Furthermore, it is found that in heave mode, the occurrence condition of the Bragg resonance shifts slightly towards the left, possibly due to the similarity between the dimensions of the floats and the separation distance[51]. A similar phenomenon is observed in the study by[52], where increasing the separation distance resulted in n_B converging to an integer.

B. Effect of base column radius

The base column radius, $R_2^{(n)}$, is also an important parameter to consider. As discussed in Section VI A, for $\omega > 0.3$ rad/s, values of $d = 14$, 11, or 10 m are recommended choices, although the optimal value of d depends on multiple parameters and optimization algorithms[45]. In this subsection, the effect of the base column radius, $R_2^{(n)}$, is investigated separately for $d = 14$ and 10 m. The comparison reveals a similar trend. Hence, $d = 10$ is selected for the following discussion. For clarity, the generic symbol R is used instead of $R_2^{(n)}$.

As illustrated in Fig.11, the surge motion RAO (X_1) is slightly affected by R, particularly at $\omega \le 1$ rad/s and $\omega \ge 1.45$ rad/s. For any specified value of X_1, a relatively large effect can be observed at 1 rad/s $\le \omega \le$ 1.45 rad/s. The peak of the frequency response of X_1 in terms of the peak value and the corresponding ω where the peak occurs is mainly affected by the R value. The peak values of the $X_1 - \omega$ curves for R ranging from 6 to 17 m vary from 0.26 to 0.31 at $\omega = 1.05$ rad/s (see Fig.11b). This indicates that the peak value of X_1 and peak frequency decrease with an increase in R. However, the decrease is very small, especially for $\omega > 1.45$ rad/s, indicating that the effect of R on X_1 is similar to the effect of d

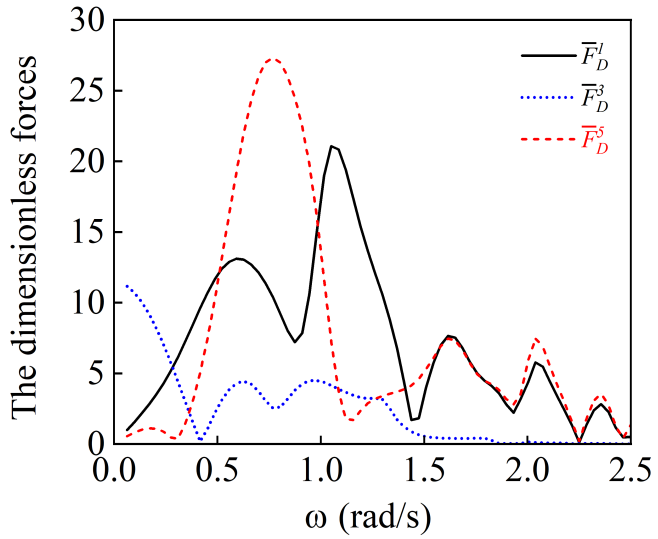

FIG. 10: The dimensionless quantities of the wave excitation per unit amplitude for the OC4 semi-submersible at a zero-degree wave heading for the surge force $\overline{F}_1^D$, heave force $\overline{F}_3^D$ and pitch moment $\overline{F}_5^D$.

described in Sec.VI A.

The variation of R with ω is more complex in the heave mode than in the above-mentioned studies. Therefore, we performed a detailed analysis using more cases, as depicted in Figs. 12 and 13. The $X_3-\omega$ curve shows that X_3 is highly sensitive to R when $\omega \leq 0.8$ rad/s, and there exists a peak in the frequency response of X_3 in the range of $0.1 \leq \omega \leq 0.8$ rad/s (see Figs. 12a and 12b). As depicted in Fig. 13, as R increases, the value of X_3 first rises and then falls. As R continues to increase, X_3 increases and then decreases again, similar to a "wave," but the amplitude of the "wave" gradually increases. Specifically, as R increases from 6 to 7.4 m, X_3 first declines from 1.98 to 1.77 at $\omega = 0.62$ rad/s (see Fig. 13a). As R continues to increase, X_3 rises and then falls after reaching a peak value of 2.39 at $R = 7.2$ m and $\omega = 0.58$ rad/s.

The rate of the increase is always smaller than the rate of the decrease. Furthermore, this change is accompanied by a decrease in the peak frequency, that is, the peak value in the $X_3-\omega$ curve shifts to the left. For a given value of ω between 0.2 to 0.3 rad/s, a sharp drop of X_3 can be observed with R ranging from 14 to 14.4 m, and a slow drop occurs in the range of $14.4 \leq R \leq 14.8$ m. Meanwhile, the peak frequency decreases more quickly in the range of $14.4 \leq R \leq 14.8$ m, leading to a new peak frequency at ∼0.25 rad/s (see Fig.13b). This similar phenomenon is repeated. For $\omega > 0.8$ rad/s, the peak value of X_3 occurs at approximately $\omega = 0.9$ rad/s and increases with R, whereas the maximum value of X_3 is smaller than 0.14 (see Fig.12c). As ω further increases to 1.4, the heave motion of the platform can be ignored.

Figs.14 and 15 depict the response of the pitch mode for different values of R and ω at $d = 10$ m and $l = 6$ m. The $X_5-\omega$ curve is highly influenced by R when $\omega \leq 0.45$ rad/s, and a peak in the frequency response of X_5 is observed within the range of $0.14 \leq \omega \leq 0.45$ rad/s. In this region, R also affects the peak of the frequency response of $X_5-\omega$ in terms of the peak value and the corresponding peak frequency. Specifically, as illustrated in Fig.14b, the peak frequency decreases with an increase in R, consistent with the behavior observed in the heave mode. The difference is that the general trend of the peak decreases with increasing R, as shown in Fig.15. For $\omega > 0.5$ rad/s, the peak value increases with R and is less than 0.82 (see Fig.14c). As ω continues to increase to 1 rad/s, the response of X_5 becomes increasingly smaller regardless of the value of R. Therefore, the performance of pitch mode is similar to that of the heave mode, except that the main peak value of the $X_5-\omega$ curve tends to decrease as R increases.

C. Effect of base column thickness

In this subsection, the effect of the base column thickness l on the motion response is discussed. The parameters $R = 12$ m in Sec.VI A and $d = 10$ m in Sec.VI B are adopted for this subsection. The base columns' thickness must be less than 10 m or the boundary must be larger than the draught depth. For clarity, the range of l is set to 1∼10 m.

The results in Fig.16 show that the surge motion RAO (X_1) is slightly influenced by l, especially for $\omega \leq 0.8$ rad/s and $\omega \geq 1.4$ rad/s. For any specified value of ω, a peak in the frequency response of X_1 occurs in the range of $1 \leq \omega \leq 1.1$ rad/s. The peak values of the $X_1-\omega$ curves for l ranging from 1 to 10 m vary from 0.32 to 0.25. This implies that the peak value of X_1 decreases as l increases. A similar variation of the peak is observed in terms of the peak value and corresponding l and ω (see Fig.16c). The data in Fig.16c also show that the peak value insignificantly changes with l, that is, less than 0.04. These results indicate that the surge motion of the platform is stable at $\omega \geq 1.4$ rad/s, as previously discussed.

Fig.17 shows the response of the motion RAO in the heave mode. The $X_3-\omega$ curve presents a more complex variation than in the surge mode, as observed in Sec.VI B. Fig.17b shows that the influence of the parameter l on X_3 is significant in the range of $0.25 \leq \omega \leq 0.5$ rad/s, particularly when the angular frequency is close to the peak frequency. The peak values of X_3 and their corresponding frequencies in the interval $\omega \in [0.3, 0.5]$ rad/s are strongly influenced by the value of l. At each peak frequency, the peak value of X_3 initially increases with l and then decreases after reaching a minimum at the same frequency. During the decrease in the peak value, the peak frequency also shifts towards lower values, i.e., the curve shifts to the left. Notably, as the peak approaches the minimum peak, the peak frequency decreases dramatically as l increases continuously. When the peak frequency decreases to a certain value, it slowly decreases again. For a given value of ω between 0.4 and 0.45 rad/s, X_3 increases rapidly from 1.9 to 3.4 as l increases from 1 to 3 m and then significantly decreases after reaching the maximum peak value at $l = 3$ m (see Fig.18a). Simultaneously, the peak frequency slowly decreases until l reaches 4.2 m. For $4.2 \leq l \leq 5$ m, the peak frequency rapidly decreases from 0.39 to 0.36 rad/s and the peak value of X_3 significantly increases again. Furthermore, as l increases, a new peak frequency emerges at $\omega = 0.35$ rad/s, and in such cases, X_3 increases from 2.4 to 4.2 as l increases from 5.8 to 7.8 m. Based on Fig. 17b for the range of $0.3 \leq \omega \leq$

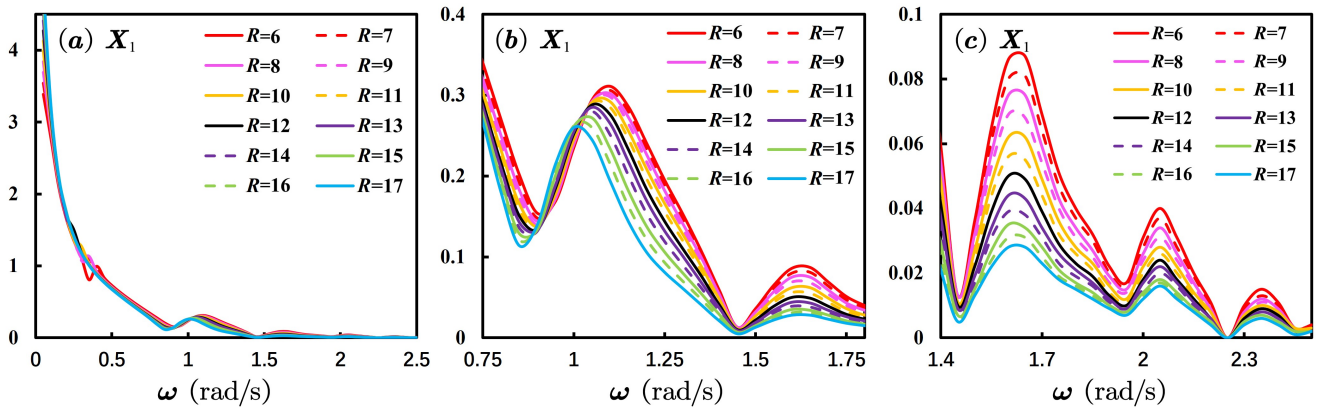

FIG. 11: Variation of the response of the surge mode in terms of the unit amplitude (m/m) with d = 10 m and l = 6 m for different base columns radii.

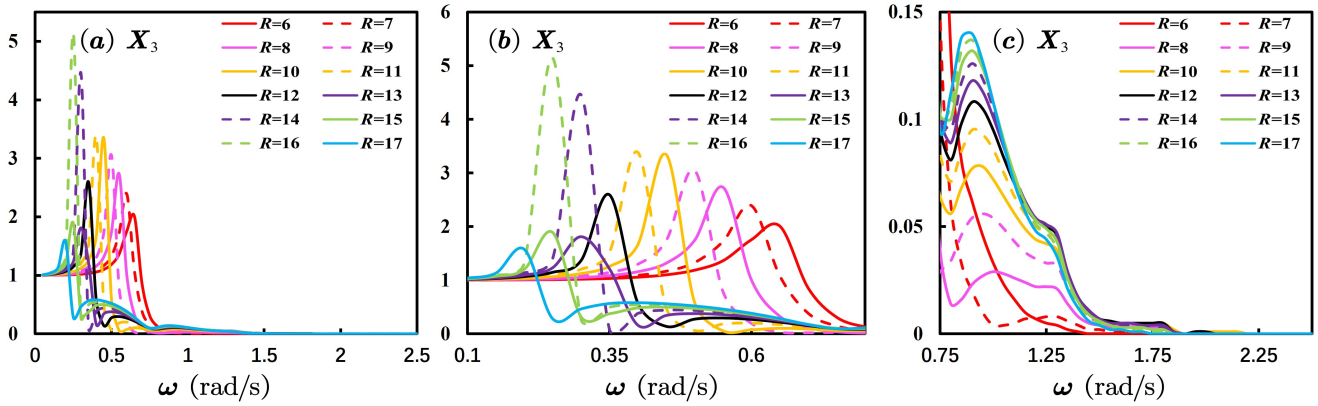

FIG. 12: Variation of the response of the heave mode in terms of the unit amplitude (m/m) with d = 10 m and l = 6 m for different base columns radii.

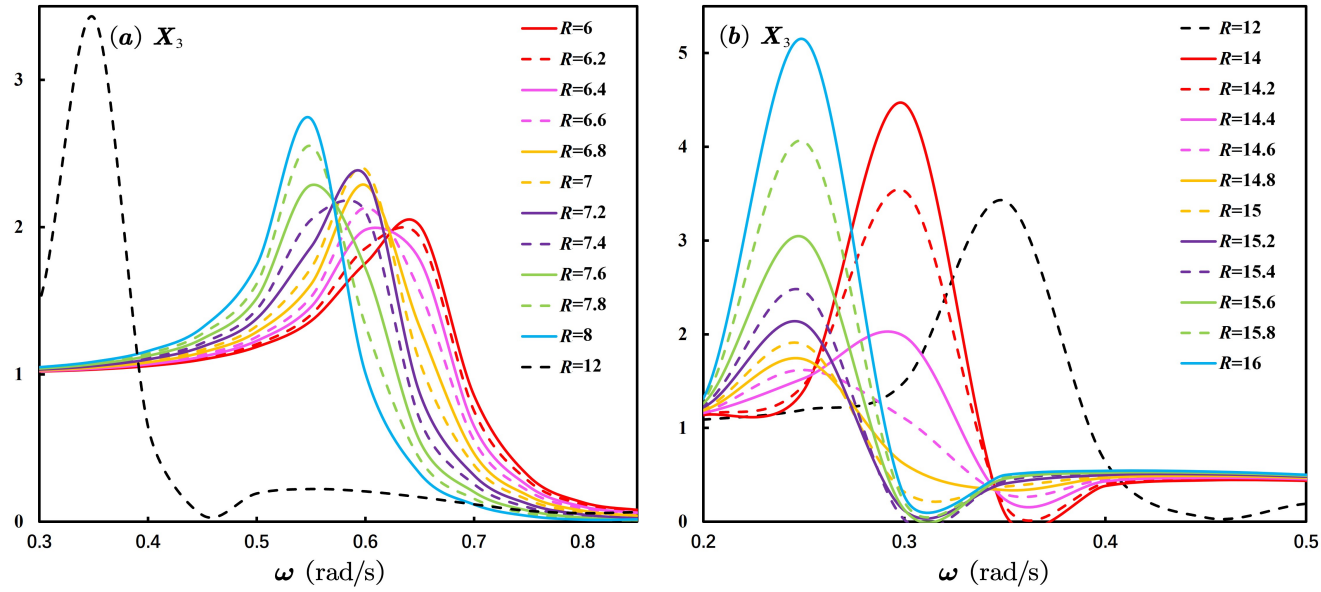

FIG. 13: Comparison of the peak value X_3 (m/m) and peak frequency for different R values with step sizes of 0.2 m, at d = 10 m and l = 6 m: (a) R = 6 - 8 m; (b) R = 14 - 16 m.

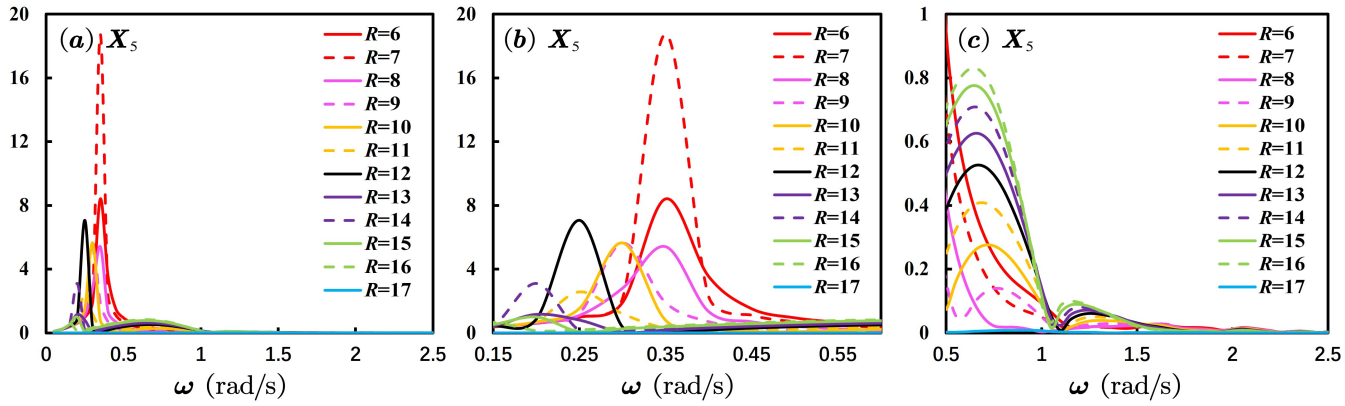

FIG. 14: Variation of the response of the pitch mode in terms of the unit amplitude (deg/m) with d = 10 m and l = 6 m for different base columns radii.

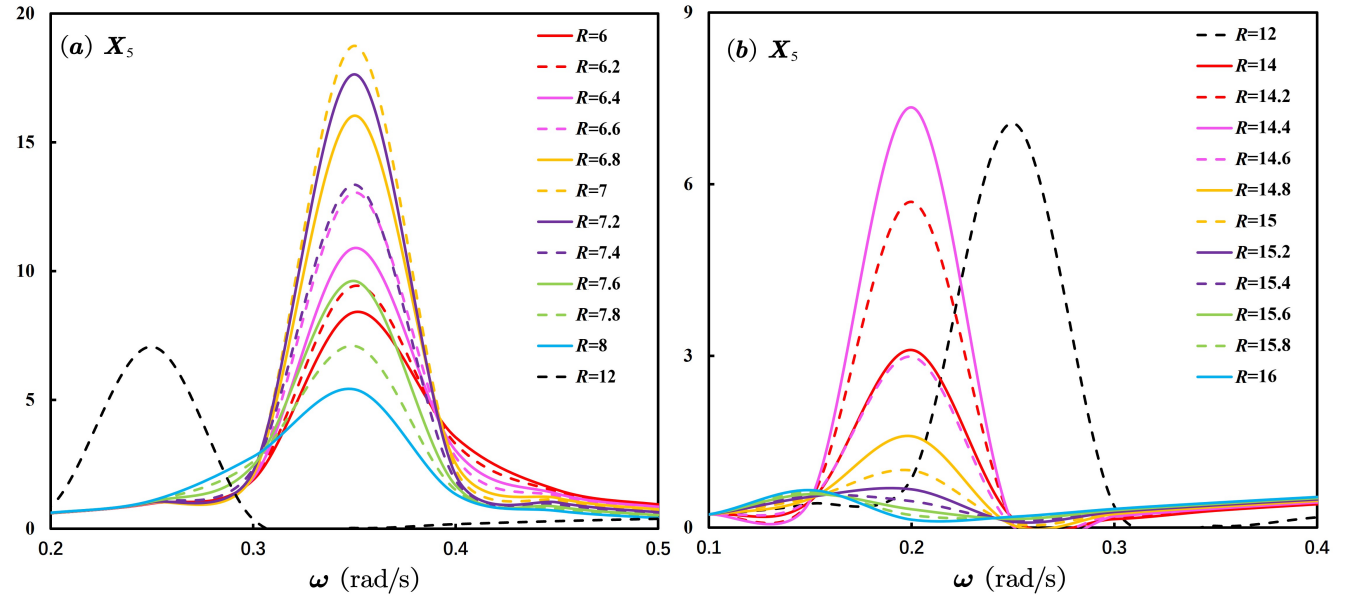

FIG. 15: Comparison of the peak value X_5 (deg/m) and peak frequency for different R values with a step size of 0.2 m, at d = 10 m and l = 6 m: (a) R = 6 - 8 m; (b) R = 14 - 16 m.

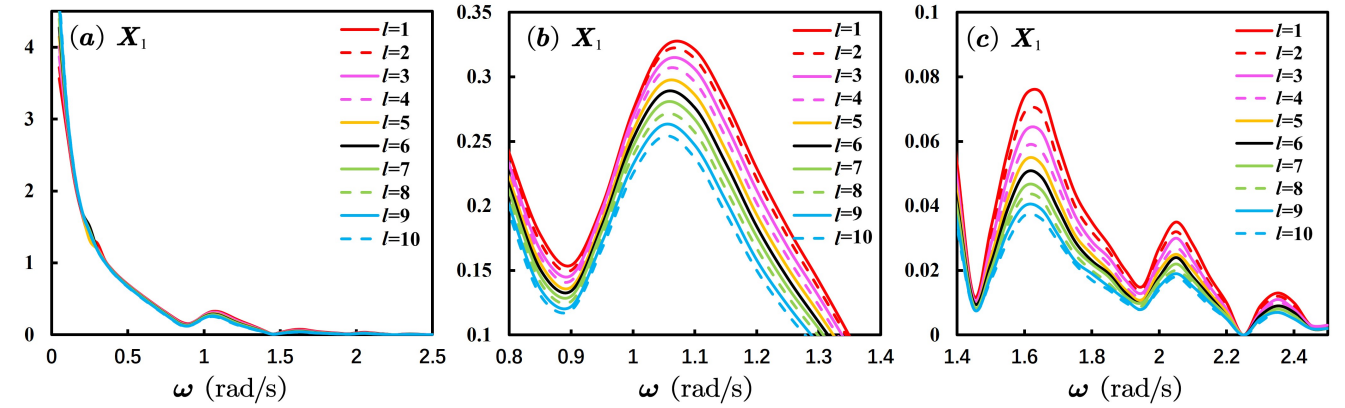

FIG. 16: Variation of the response of the surge mode in terms of the unit amplitude (m/m) with d = 10 m and R = 12 m for different base column thicknesses.

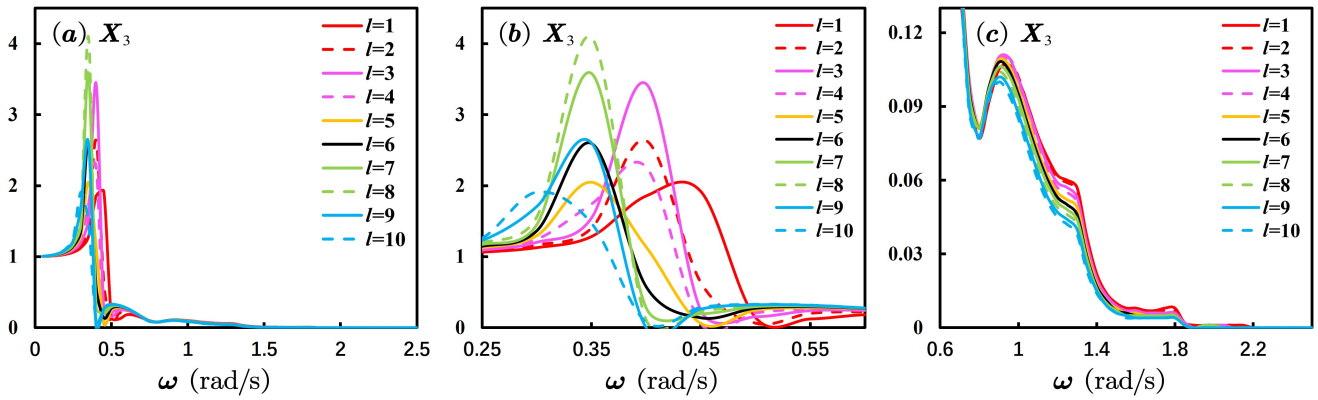

FIG. 17: Variation of the response of the heave mode in terms of the unit amplitude (m/m) with d = 10 m and R = 12 m for different base column thicknesses.

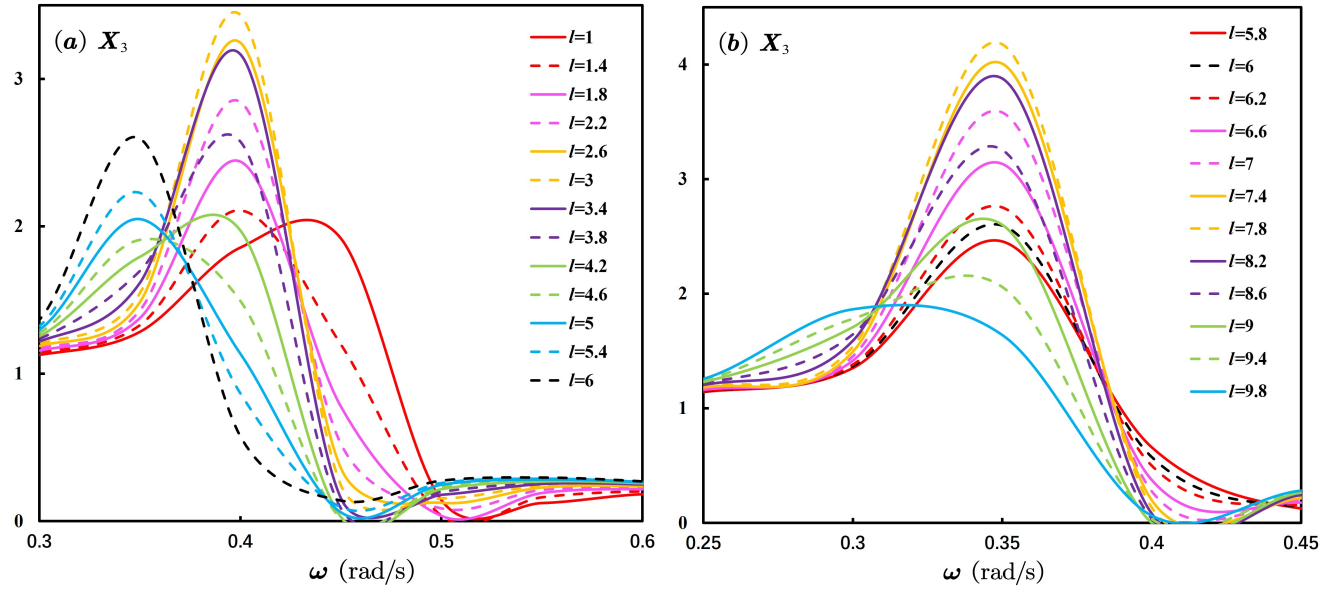

FIG. 18: Comparison of the peak response of X_3 (m/m) and peak frequency for different l values with a step size of 0.4 m, at d = 10 m and R = 12 m: (a) l = 1 - 5.4 m; (b) l = 5.8 - 9.8 m.

0.5 rad/s, the peak frequency decreases with an increase in l, and the peak value of X_3 shows a cyclical growth and decline, similar to a "wave." However, the main peak value of X_3 increases with l, which is consistent with observations made for the heave mode in Sec. VI B. For $\omega \geq 0.8$ rad/s, the peak value of X_3 is 0.11 at $\omega = 0.95$ rad/s. As ω further increases, the heave response of X_3 remains small, indicating that the hydrostatic restoring and mooring forces play a major role relative to the wave forces, and the combined effect of viscosity, added mass, and radiative damping ensure platform stability in the heave mode.

Figs. 19 and 20 present the motion response of the pitch mode for varying parameters of the thickness l and angular frequency ω. The results indicate that the behavior of the pitch mode is similar to that observed in the heave mode. As illustrated in Fig. 19, the value of X_5 is sensitive to l when $\omega \leq 0.45$ rad/s and the peak frequency in range of $0.15 \leq \omega \leq 0.35$ rad/s with $1 \leq l \leq 10$ m. In this range, l has a significant impact on both the peak frequency and peak value of X_5. The influence of l on X_5 is further illustrated in Fig. 19b, where the peak frequency decreases with an increase in l and the peak value of X_5 exhibits a "wave" pattern, with the peak value of X_5 increasing with l. For $\omega > 0.35$ rad/s, the peak value of X_5 also increases with l and the maximum value $X_5 = 0.53$ occurs at $\omega = 0.65$ rad/s (see Figs. 20a and 20b). As ω further increases to 1 rad/s, the pitch response becomes negligible, regardless of the value of l.

VII. CONCLUSIONS

A semi-analytical model for an array of marine structures is proposed in this work. The marine structures can be com-

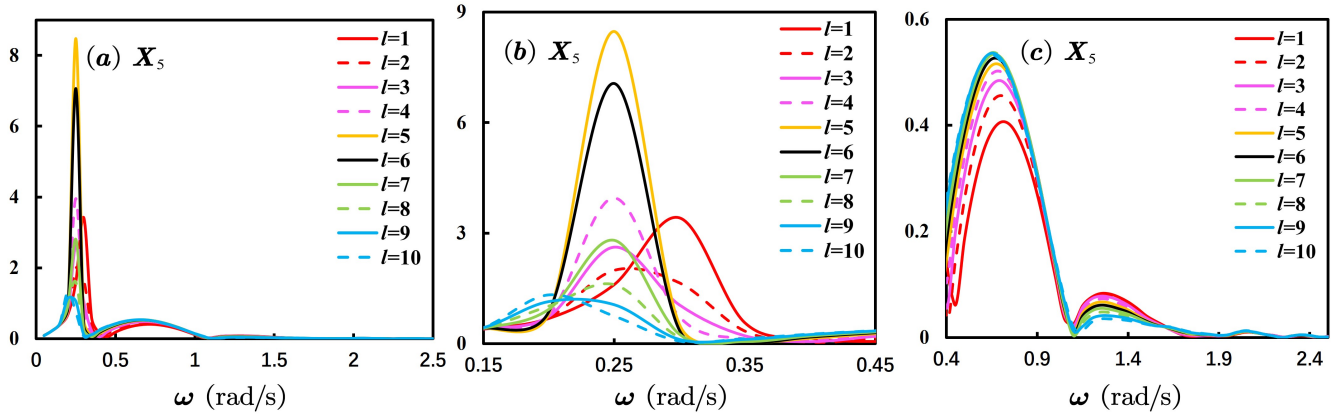

FIG. 19: Variation of the response of the pitch mode in terms of the unit amplitude (deg/m) with d = 10 m and R = 12 m for different base column thicknesses.

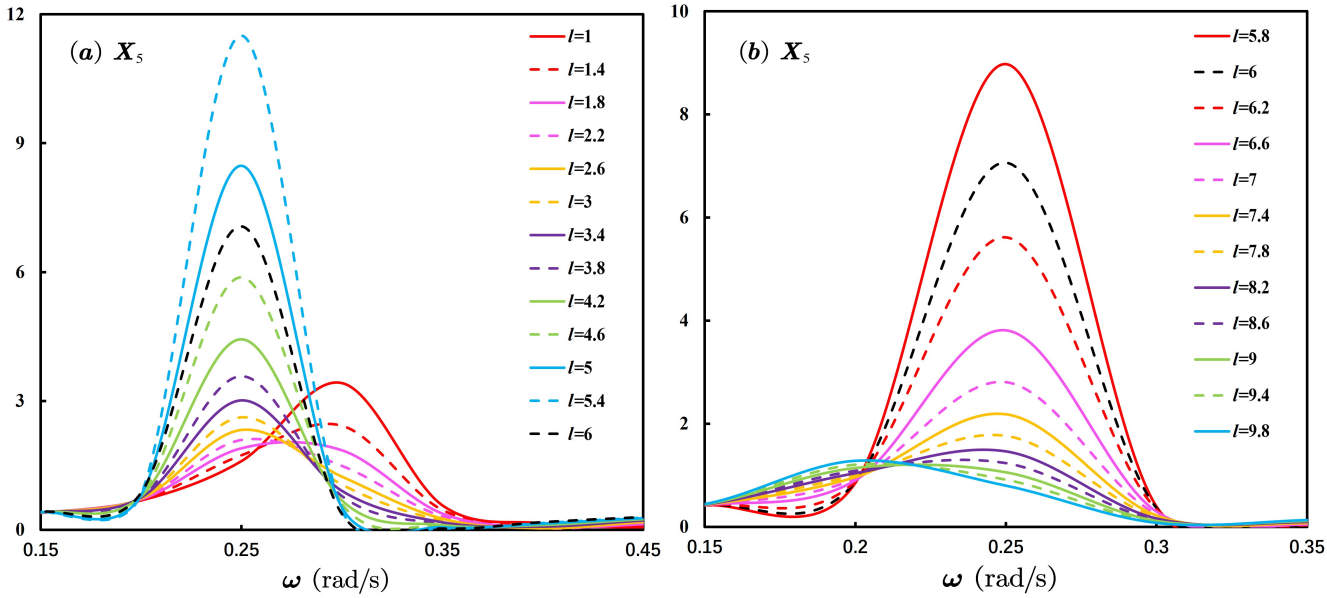

FIG. 20: Comparison of the peak response of X_5 (deg/m) and peak frequency for different l values with a step size of 0.4 m, at d = 10 m and R = 12 m: (a) l = 1 - 5.4 m; (b) l = 5.8 - 9.8 m.

posed of any number of floats, and each one can contain three different coaxial cylinders with different dimensions.

Based on the semi-analytical model, a dynamic motion equation for the response of the multiple interconnected rigid structures floating in regular waves is presented, with the study of semi-submersible FOWT being a typical application. The OC4-DeepCwind platform is adopted and investigated in this paper, including the effect of base column submergence depth, radius and thickness on the motion response of the platform, which the semi-analytical methods have not been used in this field.

A multiparameter impact analysis is conducted using the theoretical model. The results indicate that the surge motion response is insensitive to the base column depth d, radius R, and thickness l, except for the effect of d within the interval of $\omega \in [0.8, 1.15]$ rad/s. The small variation observed is primarily manifested in the peak value of the $X_1 - \omega$ curve, which varies monotonically with d, R, and l, while the peak frequency remains constant. It is noteworthy that regardless of the geometrical parameters, the platform tends to stabilize in the surge mode at $\omega \geq 1.35$ rad/s.

In contrast to the surge mode, the heave and pitch motion responses are significantly influenced by the geometrical parameters of base column depth d, radius R, and thickness l. The variations in these parameters exhibit a more complex trend, particularly in the range of $\omega \leq 0.5$rad/s. The main peak value of $X_3 - \omega$ and $X_5 - \omega$ curves shows a cyclic increase and decrease with monotonous variations in radius R and thickness l. The main peak frequency decreases with increasing R and l, while remaining insensitive to the depth of the base column d. Additionally, for $\omega \geq 1.2$ rad/s, the motion response of X_3 and X_5 decreases as ω increases, regardless of

the variation in d, R, and l.

Finally, the semi-analytical model proposed in this study has demonstrated high accuracy in predicting hydrodynamic coefficients and motion response of marine structures. In comparison to numerical models, it provides a more efficient approach. The development of this model has enabled the extension towards time-domain analysis of semi-submersible flouting foundation to study the effect of nonlinear factors. Moreover, the semi-analytical models can significantly improve the efficiency of fitness value calculation for optimization algorithms, leading to better multi-parameter optimization as demonstrated in previous studies. Overall, the interest of this work lies in the semi-analytical model itself, which is highly efficient in modelling the interaction of the wave field and can be applied in future FOWT projects. It is worth noting that this model is based on linear potential flow theory and may not be suitable for extreme wave-structure interactions.

ACKNOWLEDGEMENTS

The authors would like to acknowledge the support of the National Key R & D Program of China (Grant No. 2018YFB1501900), Shandong Provincial Natural Science Foundation (Grant No. ZR2021ZD23), National Natural Science Foundation of China (Grant No. 52071303), National Natural Science Foundation of China (Grant No. 52271297), Shandong Provincial Natural Science Foundation (Grant No. ZR2022ME002), Shandong Provincial Key Research and Development Program (Grant No. 2019JZZY010902), Taishan Scholars Program of Shandong Province (Grant No. ts20190914), S.Z. gratefully acknowledges the State Key Laboratory of Ocean Engineering, Shanghai Jiao Tong University for supporting part of this work through the Open Research Fund Program (Grant No. 1916).

AUTHOR DECLARATIONS

Conflict of Interest

The authors have no conflicts to disclose.

Author Contributions

Kai Zhu: Conceptualization, Methodology, Formal analysis, Writing – original draft, Validation, Writing – review & editing. **Siming Zheng:** Formal analysis, Investigation, Methodology, Project administration, Validation, Writing – review & editing. **Simone Michele:** Conceptualization, Methodology, Writing – review & editing. **Feifei Cao:** Investigation, Writing – review & editing. **Hongda Shi:** Formal analysis, Funding acquisition, Investigation, Project administration, Validation, Writing – review & editing. **Deborah Greaves:** Investigation, Writing – review & editing.

Data Availability Statement

Data sharing is not applicable to this article as no new data were created or analyzed in this study.

Nomenclature

A	Ambient incident wave amplitude
A_J	Displacement constraint matrix $(N_J \times 24)$
$\dot{A}_p^i$	Velocity complex amplitude of the float p oscillating in the ith mode
$a_{p,i}^{n,j}, \bar{a}_{p,i}^{n,j}$	Radiation added mass and dimensionless form of the float n in jth mode due to the Float p in ith mode
$c_{p,i}^{n,j}, \bar{c}_{p,i}^{n,j}$	Radiation damping and dimensionless form of the float n in jth mode due to the Float p in ith mode
C_d	Hydrodynamic damping matrix $(6N \times 6N)$
C_v	Linearized viscous damping matrix $(6N \times 6N)$
$d, d_1^{(n)}$	Submerged depth of the upper part of the float n
$d_2^{(n)}$	Submerged depth of the middle part of the float n
$d_3^{(n)}$	Total draft of the float n
$F_\chi^{n,j}, \bar{F}_\chi^{n,j}$	Forces or moments and dimensionless form acting on float n in jth mode
F_e	The frequency-dependent complex amplitude of exciting force array $(6N \times 1)$
F_J	The rigid force of floats vector $(N_J \times 1)$
F_m	Mooring force array $(6N \times 1)$
F_w	Wind force array $(6N \times 1)$
g	Gravitational acceleration
h	Water depth
i	Oscillating mode of float (i=1-6, which represents surge, sway, heave, roll, pitch, and yaw, respectively)
J	Vertical cut-offs number $(j = 0, 1, 2, ..., J)$
k_0	Incident wave number
$k_0^{(q)}$	Wave number for propagating mode in the region Ω_q^n
$k_j^{(q)}$	Wave number for evanescent modes in the region Ω_q^n, $(j \geq 1)$
K_s	Hydrostatic restoring matrix $(6N \times 6N)$
K_m	Mooring stiffness matrix $(6N \times 6N)$
l	Base column thickness
L	Distance between the centre of the platform and the centre of the column in the Oxy plane
M	Angular cut-offs number$(m = -M, ..., 0, ..., M)$
M_m, M_a	Floats mass matrix $(6N \times 6N)$ and add mass matrix $(6N \times 6N)$

N	Total floats number $(n = 1,2,...,N)$
N_J	Number of floats displacement constraint
R_c	The radius of the central column
$R, R_2^{(n)}$	The middle part radius of the float n
$R_1^{(n)}, R_3^{(n)}$	The upper and bottom part radius of the float n
R_0	Reference length
S	Spacing between offset column centre
X	The complex amplitude of corresponding displacements array of $(6N \times 1)$ for the N floats
X_i	Response of the motion in ith mode due to unit amplitude velocity oscillation
(x,y,z)	Cartesian coordinate system
(r,θ,z)	Cylindrical coordinate system
β	Wave incident angle
Ω_q^n	Fluid domains of the float n in region q
$(0,\theta,z_n)$	The rotation centre of the float n
ϕ	The total spatial velocity potential
ϕ_I	Incident wave potential
ϕ_D	Diffraction potential
$\phi_{p,i}$	Radiated spatial velocity potential due to unit amplitude velocity oscillation of the float p oscillating in the ith mode
δ	The Kronecker delta
ρ	Density of water
ω	Wave angular frequency

Appendix

A. Derivation process of the formulas and calculation for the unknown coefficients of both diffracted and radiated potentials

Substitute the diffracted spatial potentials in Eqs.(11)-(18) and wave incident potential given in Eq.(2b) into Eq.(22), then after multiplying both sides by $e^{-\mathrm{i}\tau\theta_n} Z_l^{(q,n)}(z)$ and integrating for $\theta_n \in [0,2\pi]$ and $z \in \left[-d_1^{(n)}, 0\right]$ and $\left[-h, -d_2^{(n)}\right]$, we get:

$$\begin{aligned}
&\tfrac{\mathrm{igA}}{\omega} I_n \mathrm{i}^\tau e^{-\mathrm{i}\tau\beta} J_\tau\left(k_0 R_2^{(n)}\right) \int_{-d_1^{(n)}}^{0} Z_0^{(0)}(z) Z_l^{(1,n)}(z) dz \\
&= \sum_{j=0}^{\infty} A_{\tau,j}^{\chi} \int_{-d_1^{(n)}}^{0} Z_j^{(0)}(z) Z_l^{(1,n)}(z) dz \\
&+ \sum_{\substack{k=1 \\ k\neq n}}^{N} \sum_{m=-\infty}^{\infty} \sum_{j=1}^{\infty} A_{m,j}^{\chi} T_{n,j,m}^{k,\tau} \int_{-d_1^{(n)}}^{0} Z_j^{(0)}(z) Z_l^{(1,n)}(z) dz \\
&-(B_{\tau,l}^{\chi} + C_{\tau,l}^{\chi}) \int_{-d_1^{(n)}}^{0} \left[Z_l^{(1,n)}(z)\right]^2 dz,
\end{aligned} \tag{A1}$$

$$\begin{aligned}
&\tfrac{\mathrm{igA}}{\omega} I_n \mathrm{i}^\tau e^{-\mathrm{i}\tau\beta} J_\tau\left(k_0 R_2^{(n)}\right) \int_{-h}^{-d_2^{(n)}} Z_0^{(0)}(z) Z_l^{(2,n)}(z) dz \\
&= \sum_{j=0}^{\infty} A_{\tau,j}^{\chi} \int_{-h}^{-d_2^{(n)}} Z_j^{(0)}(z) Z_l^{(2,n)}(z) dz \\
&+ \sum_{\substack{k=1 \\ k\neq n}}^{N} \sum_{m=-\infty}^{\infty} \sum_{j=1}^{\infty} A_{m,j}^{\chi} T_{n,j,m}^{k,\tau} \int_{-h}^{-d_2^{(n)}} Z_j^{(0)}(z) Z_l^{(2,n)}(z) dz \\
&-(D_{\tau,l}^{\chi} + E_{\tau,l}^{\chi}) \int_{-h}^{-d_2^{(n)}} \left[Z_l^{(2,n)}(z)\right]^2 dz,
\end{aligned} \tag{A2}$$

where $I_n = e^{\mathrm{i}k_0\left(\, x_n \cos\beta + y_n \sin\beta \,\right)}$ is a phase factor; $Z_l^{(q,n)}$ is the vertical function of the float n of lth mode $(l = 0,1,\cdots)$ in region Ω_q^n, which are given by

$$Z_j^{(0)}(z) = \begin{cases} \frac{\cosh[k_0(z+h)]}{\cosh(k_0 h)}, & j = 0 \\ \frac{\cos\left[k_j(z+h)\right]}{\cos\left(k_j h\right)}, & j \neq 0 \end{cases}, \tag{A3}$$

$$Z_j^{(1,n)}(z) = \begin{cases} \frac{\cosh\left[k_0^{(1)}\left(z+d_1^{(n)}\right)\right]}{\cosh(k_0^{(1)} d_1^{(n)})}, & j = 0 \\ \frac{\cos\left[k_j^{(1)}\left(z+d_1^{(n)}\right)\right]}{\cos\left(k_j^{(1)} d_1^{(n)}\right)}, & j \neq 0 \end{cases}, \tag{A4}$$

$$Z_j^{(2,n)}(z) = \begin{cases} \frac{\sqrt{2}}{2}, & j = 0 \\ \frac{\cos\left[k_j^{(2)}(z+h)\right]}{\cos\left(k_j^{(2)} h\right)}, & j \neq 0 \end{cases}, \tag{A5}$$

$$Z_j^{(3,n)}(z) = \begin{cases} \frac{\sqrt{2}}{2}, & j = 0 \\ \frac{\cos\left[k_j^{(3)}(z+h)\right]}{\cos\left(k_j^{(3)} h\right)}, & j \neq 0 \end{cases}, \tag{A6}$$

$$T_{n,j,m}^{k,\tau} = \begin{cases} \frac{H_{m-\tau}(k_0 R_{nk}) J_\tau\left(k_0 R_2^{(n)}\right) e^{\mathrm{i}(m-\tau)\theta_{nk}}}{H_m\left(k_0 R_2^{(n)}\right)}, & j = 0 \\ \frac{(-1)^\tau K_{m-\tau}\left(k_j R_{nk}\right) I_\tau\left(k_j R_2^{(n)}\right) e^{i(m-\tau)\theta_{nk}}}{K_m\left(k_j R_2^{(n)}\right)}, & j \neq 0 \end{cases}. \tag{A7}$$

Similarly, substitute the spatial potentials in Eqs.(11)-(18) and wave incident potential given in Eq.(2b) into Eq.(25), then after multiplying both sides by $e^{-\mathrm{i}\tau\theta_n} Z_l^{(0)}(z)$ and integrating for $\theta_n \in [0,2\pi]$ and $z \in [-h,0]$, we get:

$$\begin{aligned}
&A_{\tau,l}^{\chi} a_{\tau,l}^{\chi,(n)} \int_{-h}^{0} \left[Z_l^{(0)}(z)\right]^2 dz \\
&+ \sum_{\substack{k=1 \\ k\neq n}}^{N} \sum_{m=-\infty}^{\infty} A_{m,l}^{\chi} T_{n,l,m}^{\prime k,\tau} \int_{-h}^{0} \left[Z_l^{(0)}(z)\right]^2 dz \\
&-\tfrac{\mathrm{igA}}{\omega} I_n \mathrm{i}^\tau e^{-\mathrm{i}\tau\beta} \begin{bmatrix} \frac{\tau}{R_2^{(n)}} J_\tau\left(k_0 R_2^{(n)}\right) \\ -k_0 J_{\tau+1}\left(k_0 R_2^{(n)}\right) \end{bmatrix} \int_{-h}^{0} Z_0^{(0)}(z) Z_l^{(0)}(z) dz \\
&= \sum_{j=0}^{\infty} \left[B_{\tau,j}^{\chi} b_{\tau,j}^{\chi,(n)} + C_{\tau,j}^{\chi} c_{\tau,j}^{\chi,(n)}\right] \int_{-d_1^{(n)}}^{0} Z_j^{(1,n)}(z) Z_l^{(0)}(z) dz \\
&+ \sum_{j=0}^{\infty} \left[D_{\tau,j}^{\chi} d_{\tau,j}^{\chi,(n)} + E_{\tau,j}^{\chi} e_{\tau,j}^{\chi,(n)}\right] \int_{-h}^{-d_2^{(n)}} Z_j^{(2,n)}(z) Z_l^{(0)}(z) dz,
\end{aligned} \tag{A8}$$

where

$$T'^{k,\tau}_{n,j,m}=\begin{cases}\dfrac{H_{m-\tau}(k_0R_{nk})}{H_m\left(k_0R_2^{(n)}\right)}\begin{bmatrix}\frac{\tau}{R_2^{(n)}}J_\tau\left(k_0R_2^{(n)}\right)\\ -k_0J_{\tau+1}\left(k_0R_2^{(n)}\right)\end{bmatrix}e^{\mathrm{i}(m-\tau)\theta_{nk}}, & j=0\\ \dfrac{(-1)^\tau K_{m-\tau}\left(k_jR_{nk}\right)}{K_m\left(k_jR_2^{(n)}\right)}\begin{bmatrix}\frac{\tau}{R_2^{(n)}}I_\tau\left(k_jR_2^{(n)}\right)\\ +k_jI_{\tau+1}\left(k_jR_2^{(n)}\right)\end{bmatrix}e^{\mathrm{i}(m-\tau)\theta_{nk}}, & j\neq 1\end{cases}, \tag{A9}$$

$$a^{\chi,(n)}_{\tau,j}=\begin{cases}\dfrac{\tau}{R_2^{(n)}}-\dfrac{k_0H_{\tau+1}\left(k_0R_2^{(n)}\right)}{H_\tau\left(k_0R_2^{(n)}\right)}, & j=0\\ \dfrac{\tau}{R_2^{(n)}}-\dfrac{k_jK_{\tau+1}\left(k_jR_2^{(n)}\right)}{K_\tau\left(k_jR_2^{(n)}\right)}, & j\neq 0\end{cases}, \tag{A10}$$

$$b^{\chi,(n)}_{\tau,j}=\begin{cases}\dfrac{\tau}{R_2^{(n)}}-\dfrac{k_0^{(1)}J_{\tau+1}\left(k_0^{(1)}R_2^{(n)}\right)}{J_\tau\left(k_0^{(1)}R_2^{(n)}\right)}, & j=0\\ \dfrac{\tau}{R_2^{(n)}}+\dfrac{k_j^{(1)}I_{\tau+1}\left(k_j^{(1)}R_2^{(n)}\right)}{I_\tau\left(k_j^{(1)}R_2^{(n)}\right)}, & j\neq 0\end{cases}, \tag{A11}$$

$$c^{\chi,(n)}_{\tau,j}=\begin{cases}\dfrac{\tau}{R_2^{(n)}}-\dfrac{k_0^{(1)}H_{\tau+1}\left(k_0^{(1)}R_2^{(n)}\right)}{H_\tau\left(k_0^{(1)}R_2^{(n)}\right)}, & j=0\\ \dfrac{\tau}{R_2^{(n)}}-\dfrac{k_j^{(1)}K_{\tau+1}\left(k_j^{(1)}R_2^{(n)}\right)}{K_\tau\left(k_j^{(1)}R_2^{(n)}\right)}, & j\neq 0\end{cases}, \tag{A12}$$

$$d^{\chi,(n)}_{\tau,j}=\begin{cases}\dfrac{|\tau|}{R_2^{(n)}}, & j=0\\ \dfrac{\tau}{R_2^{(n)}}+\dfrac{k_j^{(2)}I_{\tau+1}\left(k_j^{(2)}R_2^{(n)}\right)}{I_\tau\left(k_j^{(2)}R_2^{(n)}\right)}, & j\neq 0\end{cases}, \tag{A13}$$

$$e^{\chi,(n)}_{\tau,j}=\begin{cases}-\dfrac{|\tau|}{R_2^{(n)}},\tau\neq 0;\dfrac{1}{R_2^{(n)}},\tau=0, & j=0\\ \dfrac{\tau}{R_2^{(n)}}-\dfrac{k_j^{(2)}K_{\tau+1}\left(k_j^{(2)}R_2^{(n)}\right)}{K_\tau\left(k_j^{(2)}R_2^{(n)}\right)}, & j\neq 0\end{cases}. \tag{A14}$$

Substitute the spatial potentials in Eqs.(13)-(21) into Eqs.(23), (24) and (26), then after multiplying both sides by $e^{-\mathrm{i}m\theta_n}Z_l^{(q,n)}(z)$ and integrating for $\theta_n\in[0,2\pi]$ and $z\in\left[-h,-d_3^{(n)}\right]$, $\left[-h,-d_2^{(n)}\right]$, $\left[-d_1^{(n)},0\right]$, we get:

$$\begin{aligned}&\sum_{j=0}^{\infty}\left[D^\chi_{m,j}d'^{\chi,(n)}_{m,j}+E^\chi_{m,j}e'^{\chi,(n)}_{m,j}\right]\int_{-h}^{-d_3^{(n)}}Z_0^{(2,n)}(z)Z_l^{(3,n)}(z)dz\\&=F^\chi_{m,l}\int_{-h}^{-d_3^{(n)}}\left[Z_l^{(3,n)}(z)\right]^2dz,\end{aligned} \tag{A15}$$

$$\begin{aligned}&\left[D^\chi_{m,l}d''^{\chi,(n)}_{m,l}+E^\chi_{m,l}e''^{\chi,(n)}_{m,l}\right]\int_{-h}^{-d_2^{(n)}}\left[Z_l^{(2,n)}(z)\right]^2dz\\&=F^\chi_{m,0}\frac{|m|}{R_3^{(n)}}\int_{-h}^{-d_3^{(n)}}Z_0^{(3,n)}(z)Z_l^{(2,n)}(z)dz\\&+\sum_{j=1}^{\infty}F^\chi_{m,j}\left(\frac{m}{R_3^{(n)}}-\frac{k_j^{(3)}I_{m+1}\left(k_j^{(3)}R_3^{(n)}\right)}{I_m\left(k_j^{(3)}R_3^{(n)}\right)}\right)\int_{-h}^{-d_3^{(n)}}Z_j^{(3,n)}(z)Z_l^{(2,n)}(z)dz,\end{aligned} \tag{A16}$$

$$\left[B^\chi_{m,l}b'^{\chi,(n)}_{m,l}+C^\chi_{m,l}c'^{\chi,(n)}_{m,l}\right]\int_{-d_1^{(n)}}^{0}\left[Z_l^{(1,n)}(z)\right]^2dz=0, \tag{A17}$$

$$d'^{\chi,(n)}_{m,j}=\begin{cases}\left(\dfrac{R_3^{(n)}}{R_2^{(n)}}\right)^{|m|}, & j=0\\ \dfrac{I_m\left(k_j^{(2)}R_3^{(n)}\right)}{I_m\left(k_j^{(2)}R_2^{(n)}\right)}, & j\neq 0\end{cases}, \tag{A18}$$

$$\mathrm{e}'^{\chi,(n)}_{m,j}=\begin{cases}\begin{cases}\left(\dfrac{R_3^{(n)}}{R_2^{(n)}}\right)^{-|m|}, & m\neq 0\\ 1+\ln\left(\dfrac{R_3^{(n)}}{R_2^{(n)}}\right), & m=0,\end{cases}, & j=0\\ \dfrac{K_m\left(k_j^{(2)}R_3^{(n)}\right)}{K_m\left(k_j^{(2)}R_2^{(n)}\right)}, & j\neq 0\end{cases}, \tag{A19}$$

$$d''^{\chi,(n)}_{m,j}=\begin{cases}\dfrac{|m|\left(R_3^{(n)}\right)^{|m|-1}}{\left(R_2^{(n)}\right)^{|m|}}, & j=0\\ \dfrac{mI_m\left(k_j^{(2)}R_3^{(n)}\right)-R_3^{(n)}k_j^{(2)}I_{m+1}\left(k_j^{(2)}R_3^{(n)}\right)}{R_3^{(n)}I_m\left(k_j^{(2)}R_2^{(n)}\right)}, & j\neq 0\end{cases}, \tag{A20}$$

$$\mathrm{e}''^{\chi,(n)}_{m,j}=\begin{cases}\dfrac{-|m|\left(R_3^{(n)}\right)^{-|m|-1}}{\left(R_2^{(n)}\right)^{-|m|}},m\neq 0;\dfrac{1}{R_3^{(n)}},m=0, & j=0\\ \dfrac{mK_m\left(k_j^{(2)}R_3^{(n)}\right)-R_3^{(n)}k_j^{(2)}K_{m+1}\left(k_j^{(2)}R_3^{(n)}\right)}{R_3^{(n)}K_m\left(k_j^{(2)}R_2^{(n)}\right)}, & j\neq 0\end{cases}, \tag{A21}$$

$$b'^{\chi,(n)}_{m,j}=\begin{cases}\dfrac{mJ_m\left(k_0^{(1)}R_1^{(n)}\right)-R_1^{(n)}k_0^{(1)}J_{m+1}\left(k_0^{(1)}R_1^{(n)}\right)}{R_1^{(n)}J_m\left(k_0^{(1)}R_2^{(n)}\right)}, & j=0\\ \dfrac{mI_m\left(k_j^{(1)}R_1^{(n)}\right)+R_1^{(n)}k_j^{(1)}I_{m+1}\left(k_j^{(1)}R_1^{(n)}\right)}{R_1^{(n)}I_m\left(k_j^{(1)}R_2^{(n)}\right)}, & j\neq 0\end{cases}, \tag{A22}$$

$$\mathrm{c}'^{\chi,(n)}_{m,j}=\begin{cases}\dfrac{mH_m\left(k_0^{(1)}R_1^{(n)}\right)-R_1^{(n)}k_0^{(1)}H_{m+1}\left(k_0^{(1)}R_1^{(n)}\right)}{R_1^{(n)}H_m\left(k_0^{(1)}R_2^{(n)}\right)}, & j=0\\ \dfrac{mK_m\left(k_j^{(1)}R_1^{(n)}\right)-R_1^{(n)}k_j^{(1)}K_{m+1}\left(k_j^{(1)}R_1^{(n)}\right)}{R_1^{(n)}K_m\left(k_j^{(1)}R_2^{(n)}\right)}, & j\neq 0\end{cases}. \tag{A23}$$

For the radiated spatial potentials due to float oscillation of all the floats in six freedom, similar expressions can also be derived. Derivation shows that the diffracted and radiated spatial potentials share the same M and J order linear complex coefficient matrix, hence wave diffraction and wave radiation problems can be solved simultaneously.

B. The brief derivation and the final complicated formulae for calculation of forces and moments

(1) For $j=1,2$, $F_\chi^{n,j}$ can be expressed as

$$F_\chi^{n,j}=-\pi\omega^2\rho\times \left[\begin{array}{l} R_1^{(n)}\left[P_0\frac{\tanh\left(k_0^{(1)}d_1^{(n)}\right)}{k_0^{(1)}}+P_1\frac{\tan\left(k_j^{(1)}d_1^{(n)}\right)}{k_j^{(1)}}\right] \\ +R_2^{(n)}\left[\begin{array}{l} Q_0\frac{\sinh\left[k_0\left(h-d_1^{(n)}\right)\right]-\sinh\left[k_0\left(h-d_2^{(n)}\right)\right]}{k_0\cosh(k_0h)} \\ +Q_1\frac{\sin\left[k_j\left(h-d_1^{(n)}\right)\right]-\sin\left[k_j\left(h-d_2^{(n)}\right)\right]}{k_j\cos\left(k_jh\right)}\end{array}\right] \\ +R_3^{(n)}\left[\frac{Y_0}{\sqrt{2}}\left(d_3^{(n)}-d_2^{(n)}\right)+Y_1\frac{\sin\left[k_j^{(2)}\left(h-d_3^{(n)}\right)\right]}{k_j^{(2)}\cos\left(k_j^{(2)}h\right)}\right]\end{array}\right]+f_\chi^{n,j}, \tag{B1}$$

where

$$P_a=\begin{cases}\left[\begin{array}{l}-B_{-1,0}^\chi\frac{J_{-1}\left(k_0^{(1)}R_1^{(n)}\right)}{J_{-1}\left(k_0^{(1)}R_2^{(n)}\right)}+B_{1,0}^\chi\frac{J_1\left(k_0^{(1)}R_1^{(n)}\right)}{J_1\left(k_0^{(1)}R_2^{(n)}\right)} \\ -C_{-1,0}^\chi\frac{H_{-1}\left(k_0^{(1)}R_1^{(n)}\right)}{H_{-1}\left(k_0^{(1)}R_2^{(n)}\right)}+C_{1,0}^\chi\frac{H_1\left(k_0^{(1)}R_1^{(n)}\right)}{H_1\left(k_0^{(1)}R_2^{(n)}\right)}\end{array}\right], a=0 \\ \sum_{j=1}^{\infty}\left[\begin{array}{l}(-1)^{j+1}B_{-1,j}^\chi\frac{I_{-1}\left(k_j^{(1)}R_1^{(n)}\right)}{I_{-1}\left(k_j^{(1)}R_2^{(n)}\right)} \\ +(-1)^{j+1}C_{-1,j}^\chi\frac{K_{-1}\left(k_j^{(1)}R_1^{(n)}\right)}{K_{-1}\left(k_j^{(1)}R_2^{(n)}\right)} \\ +B_{1,j}^\chi\frac{I_1\left(k_j^{(1)}R_1^{(n)}\right)}{I_1\left(k_j^{(1)}R_2^{(n)}\right)}+C_{1,j}^\chi\frac{K_1\left(k_j^{(1)}R_1^{(n)}\right)}{K_1\left(k_j^{(1)}R_2^{(n)}\right)}\end{array}\right], a=1\end{cases}, \tag{B2}$$

$$Q_a=\begin{cases}-A_{-1,0}^\chi+A_{1,0}^\chi, & a=0 \\ \sum_{j=1}^{\infty}\left[(-1)^{j+1}A_{-1,j}^\chi+A_{1,j}^\chi\right], & a=1\end{cases}, \tag{B3}$$

$$Y_a=\begin{cases}\left[\begin{array}{l}-D_{-1,0}^\chi\frac{R_3^{(n)}}{R_2^{(n)}}+D_{1,0}^\chi\frac{R_3^{(n)}}{R_2^{(n)}} \\ -E_{-1,0}^\chi\frac{R_3^{(n)}}{R_2^{(n)}}+E_{1,0}^\chi\frac{R_3^{(n)}}{R_2^{(n)}}\end{array}\right], & a=0 \\ \sum_{j=1}^{\infty}\left[\begin{array}{l}(-1)^{j+1}D_{-1,j}^\chi\frac{I_{-1}\left(k_j^{(2)}R_3^{(n)}\right)}{I_{-1}\left(k_j^{(2)}R_2^{(n)}\right)} \\ +(-1)^{j+1}E_{-1,j}^\chi\frac{K_{-1}\left(k_j^{(2)}R_3^{(n)}\right)}{K_{-1}\left(k_j^{(2)}R_2^{(n)}\right)} \\ +D_{1,j}^\chi\frac{I_1\left(k_j^{(2)}R_3^{(n)}\right)}{I_1\left(k_j^{(2)}R_2^{(n)}\right)}+E_{1,j}^\chi\frac{K_1\left(k_j^{(2)}R_3^{(n)}\right)}{K_1\left(k_j^{(2)}R_2^{(n)}\right)}\end{array}\right], & a=1\end{cases}, \tag{B4}$$

when χ = 'D' and $j=1,2$, $f_D^{n,j}$ can be expressed as

$$f_D^{n,j}=\frac{1}{k_0\cosh(k_0h)}\left[(-1)^j\mathrm{i}e^{\mathrm{i}\beta}J_{-1}\left(k_0R_2^{(n)}\right)+\mathrm{i}e^{-\mathrm{i}\beta}J_1\left(k_0R_2^{(n)}\right)\right] \times\left[\sinh\left(k_0\left(h-d_1^{(n)}\right)\right)-\sinh\left(k_0\left(h-d_2^{(n)}\right)\right)\right], \tag{B5}$$

when χ = 'p,i' and $j=1,2$, $f_{p,i}^{n,j}$ can be expressed as

$$f_{p,i}^{n,j}=\begin{cases}0, \quad \text{others} \\ (-1)^j\omega^2\rho\pi\times \left[\begin{array}{l}\left(R_1^{(n)}\right)^2d_1^{(n)}\left(\frac{d_1^{(n)}}{2}-\frac{g}{\omega^2}\right) \\ +\frac{\left(R_3^{(n)}\right)^2}{8\left(h-d_2^{(n)}\right)}\left[\begin{array}{l}\frac{4}{3}\left[\begin{array}{l}\left(h-d_3^{(n)}\right)^3 \\ -\left(h-d_2^{(n)}\right)^3\end{array}\right] \\ +\left(R_3^{(n)}\right)^2\left(d_3^{(n)}-d_2^{(n)}\right)\end{array}\right]\end{array}\right], \\ \quad n=p \text{ and } j=1,i=5 \text{ or } j=2,i=4\end{cases}. \tag{B6}$$

(2) For $j=3$, $F_\chi^{n,j}$ can be expressed as

$$F_\chi^{n,j}=2\pi\omega^2\rho\times\left[\begin{array}{l}S_0\frac{\sqrt{2}}{2}+\frac{F_{0,0}^\chi\left(R_3^{(n)}\right)^2}{2\sqrt{2}}+S_1\frac{\cos\left(k_j^{(2)}\left(h-d_2^{(n)}\right)\right)}{\cos\left(k_j^{(2)}h\right)}-T_0\frac{1}{\cosh\left(k_0^{(1)}d_1^n\right)}+T_1\frac{1}{\cos\left(k_j^{(1)}d_1^n\right)} \\ +\sum_{j=1}^{\infty}F_{0,j}^\chi\frac{R_3^{(n)}I_1\left(k_j^{(3)}R_3^{(n)}\right)}{k_j^{(3)}I_0\left(k_j^{(3)}R_3^{(n)}\right)}\frac{\cos\left(k_j^{(3)}\left(h-d_3^{(n)}\right)\right)}{\cos\left(k_j^{(3)}h\right)}\end{array}\right]+f_\chi^{n,j}, \tag{B7}$$

where

$$S_a=\begin{cases}\frac{D_{0,0}^\chi}{2}\left(R_2^{(n)}-R_3^{(n)}\right)^2+\frac{E_{0,0}^\chi}{4}\left[\left(R_2^{(n)}\right)^2-\left(R_3^{(n)}\right)^2-2\left(R_3^{(n)}\right)^2\ln\left(\frac{R_3^{(n)}}{R_2^{(n)}}\right)\right], & a=0 \\ \sum_{j=1}^{\infty}\left[D_{0,j}^\chi\left[\frac{R_2^{(n)}I_1\left(k_j^{(2)}R_2^{(n)}\right)-R_3^{(n)}I_1\left(k_j^{(2)}R_3^{(n)}\right)}{k_j^{(2)}I_0\left(k_j^{(2)}R_2^{(n)}\right)}\right]+E_{0,j}^\chi\left[\frac{R_3^{(n)}K_1\left(k_j^{(2)}R_3^{(n)}\right)-R_2^{(n)}K_1\left(k_j^{(2)}R_2^{(n)}\right)}{k_j^{(2)}K_0\left(k_j^{(2)}R_2^{(n)}\right)}\right]\right], & a=1\end{cases}, \tag{B8}$$

$$T_a=\begin{cases} B_{0,0}^{\chi}\frac{R_2^{(n)}J_1\left(k_0^{(1)}R_2^{(n)}\right)-R_1^{(n)}J_1\left(k_0^{(1)}R_1^{(n)}\right)}{k_0^{(1)}J_0\left(k_0^{(1)}R_2^{(n)}\right)}+C_{0,0}^{\chi}\frac{R_2^{(n)}H_1\left(k_0^{(1)}R_2^{(n)}\right)-R_1^{(n)}H_1\left(k_0^{(1)}R_1^{(n)}\right)}{k_0^{(1)}H_0\left(k_0^{(1)}R_2^{(n)}\right)}, & a=0 \\ \sum\limits_{j=1}^{\infty}\left[B_{0,j}^{\chi}\frac{R_2^{(n)}I_1\left(k_j^{(1)}R_2^{(n)}\right)-R_1^{(n)}I_1\left(k_j^{(1)}R_1^{(n)}\right)}{k_j^{(1)}I_0\left(k_j^{(1)}R_2^{(n)}\right)}+C_{0,j}^{\chi}\frac{R_1^{(n)}K_1\left(k_j^{(1)}R_1^{(n)}\right)-R_2^{(n)}K_1\left(k_j^{(1)}R_2^{(n)}\right)}{k_j^{(1)}K_0\left(k_j^{(1)}R_2^{(n)}\right)}\right], & a=1 \end{cases}, \tag{B9}$$

when χ = 'D' and $j=3$, $f_{\chi}^{n,j}$ vanishes; when and χ = 'p,i', $f_{\chi}^{n,j}$ can be expressed as

$$f_{p,i}^{n,j}=\begin{cases} 0, \text{ others} \\ \frac{\pi\omega^2\rho}{2}\left[\begin{array}{l}\left(h-d_2^{(n)}\right)\left[\left(R_2^{(n)}\right)^2-\left(R_3^{(n)}\right)^2\right]-\frac{\left(R_2^{(n)}\right)^4-\left(R_3^{(n)}\right)^4}{4\left(h-d_2^{(n)}\right)}-\frac{\left(R_3^{(n)}\right)^4}{4\left(h-d_3^{(n)}\right)} \\ +\left(h-d_3^{(n)}\right)\left(R_3^{(n)}\right)^2-2\left(\frac{g}{\omega^2}-d_1^{(n)}\right)\left(\left(R_2^{(n)}\right)^2-\left(R_3^{(n)}\right)^2\right)\end{array}\right], & n=p \text{ and } j=3, i=3 \end{cases}. \tag{B10}$$

(3) For $j=4,5$, $F_{\chi}^{n,j}=F_{\chi,2}^{\prime\, n,j}+F_{\chi,1}^{\prime\, n,j}+F_{\chi,3}^{\prime\, n,j}-(F_{\chi,3}^{\prime\prime\, n,j}+F_{\chi,4}^{\prime\prime\, n,j}+F_{\chi,2}^{\prime\prime\, n,j})+f_{\chi}^{n,j}$, each component can be expressed as

$$F_{\chi,2}^{\prime\, n,j}=f_cR_1^{(n)}\left[P_0\frac{1-\cosh\left(k_0^{(1)}d_1^{(n)}\right)-z_nk_0^{(1)}\sinh\left(k_0^{(1)}d_1^{(n)}\right)}{\left(k_0^{(1)}\right)^2\cosh\left(k_0^{(1)}d_1^{(n)}\right)}+P_1\frac{\cos\left(k_j^{(1)}d_1^{(n)}\right)-z_nk_j^{(1)}\sin\left(k_0^{(1)}d_1^{(n)}\right)-1}{\left(k_j^{(1)}\right)^2\cos\left(k_j^{(1)}d_1^{(n)}\right)}\right], \tag{B11}$$

$$F_{\chi,1}^{\prime\, n,j}=f_cR_2^{(n)}\left[\begin{array}{l}\frac{Q_0}{{k_0}^2\cosh(k_0h)}\left[\begin{array}{l}\cosh\left(k_0\left(h-d_2^{(n)}\right)\right)+k_0\left(d_2^{(n)}+z_n\right)\sinh\left(k_0\left(h-d_2^{(n)}\right)\right) \\ -\cosh\left(k_0\left(h-d_1^{(n)}\right)\right)-k_0\left(d_1^{(n)}+z_n\right)\sinh\left(k_0\left(h-d_1^{(n)}\right)\right)\end{array}\right] \\ +\frac{Q_1}{{k_j}^2\cos\left(k_jh\right)}\left[\begin{array}{l}\cos\left(k_j\left(h-d_1^{(n)}\right)\right)-k_j\left(d_1^{(n)}+z_n\right)\sin\left(k_j\left(h-d_1^{(n)}\right)\right) \\ -\cos\left(k_j\left(h-d_2^{(n)}\right)\right)+k_j\left(d_2^{(n)}+z_n\right)\sin\left(k_j\left(h-d_2^{(n)}\right)\right)\end{array}\right]\end{array}\right], \tag{B12}$$

$$F_{\chi,3}^{\prime\, n,j}=f_cR_3^{(n)}\left[\begin{array}{l}\frac{Y_0}{2\sqrt{2}}\left[\left(d_2^{(n)}\right)^2-\left(d_3^{(n)}\right)^2-2z_n\left(d_3^{(n)}-d_2^{(n)}\right)\right] \\ +\frac{Y_1}{\left(k_j^{(2)}\right)^2\cos\left(k_j^{(2)}h\right)}\left[\begin{array}{l}\cos\left(k_j^{(2)}\left(h-d_2^{(n)}\right)\right)-k_j^{(2)}\left(d_2^{(n)}+z_n\right)\sin\left(k_j^{(2)}\left(h-d_2^{(n)}\right)\right) \\ -\cos\left(k_j^{(2)}\left(h-d_3^{(n)}\right)\right)+k_j^{(2)}\left(d_3^{(n)}+z_n\right)\sin\left(k_j^{(2)}\left(h-d_3^{(n)}\right)\right)\end{array}\right]\end{array}\right], \tag{B13}$$

$$F_{\chi,3}^{\prime\prime\, n,j}+F_{\chi,4}^{\prime\prime\, n,j}+F_{\chi,2}^{\prime\prime\, n,j}=f_c\left[U_0+U_1\frac{\cos\left(k_j^{(2)}\left(h-d_2^{(n)}\right)\right)}{\cos\left(k_j^{(2)}h\right)}+V_0\frac{\sqrt{2}\left(R_3^{(n)}\right)^3}{8}+V_1\frac{\cos\left(k_j^{(3)}\left(h-d_3^{(n)}\right)\right)}{\cos\left(k_j^{(3)}h\right)}-\frac{W_0}{\cosh\left(k_0^{(1)}d_1^{(n)}\right)}-\frac{W_1}{\cos\left(k_j^{(1)}d_1^{(n)}\right)}\right], \tag{B14}$$

when χ = 'D' and $j=4,5$, $f_D^{n,j}$ can be expressed as:

$$f_D^{n,j}=\frac{2f_c\mathrm{i}R_2^{(n)}\cosh(\mathrm{i}\beta)J_1(k_0R_2^{(n)})}{{k_0}^2\cosh(k_0h)}\left[\begin{array}{l}\cosh\left(k_0\left(h-d_2^{(n)}\right)\right)+k_0\left(d_2^{(n)}+z_n\right)\sinh\left(k_0\left(h-d_2^{(n)}\right)\right) \\ -\cosh\left(k_0\left(h-d_1^{(n)}\right)\right)-k_0\left(d_1^{(n)}+z_n\right)\sinh\left(k_0\left(h-d_1^{(n)}\right)\right)\end{array}\right], \tag{B15}$$

when χ = 'p,i' and $j=4,5$, $f_{p,i}^{n,j}$ can be expressed as:

$$m_{p,i}^{n,j}=\begin{cases}0, \quad \text{others} \\ (-1)^j\omega^2\rho\pi\left[\begin{array}{l}\left[\begin{array}{l}\left(R_1^{(n)}d_1^{(n)}\right)^2\left(\frac{d_1^{(n)}}{3}-\frac{g}{2\omega^2}\right)+\frac{h\left(R_3^{(n)}\right)^2}{3\left(h-d_2^{(n)}\right)}\left(\left(d_3^{(n)}\right)^3-\left(d_2^{(n)}\right)^3\right) \\ +\frac{\left(d_2^{(n)}\right)^4-\left(R_3^{(n)}d_3^{(n)}\right)^2}{8\left(h-d_2^{(n)}\right)}\left(\left(d_2^{(n)}\right)^2+\left(d_3^{(n)}\right)^2+2h^2-\frac{\left(R_3^{(n)}\right)^2}{2}\right)\end{array}\right] \\ +\frac{1}{8}\left[\begin{array}{l}\left(\left(R_2^{(n)}\right)^4-\left(R_3^{(n)}\right)^4\right)\left(h-d_2^{(n)}\right)-\frac{\left(R_2^{(n)}\right)^6-\left(R_3^{(n)}\right)^6}{6\left(h-d_2^{(n)}\right)}-\frac{\left(R_3^{(n)}\right)^6}{6\left(h-d_3^{(n)}\right)} \\ +\left(R_3^{(n)}\right)^4\left(h-d_3^{(n)}\right)+2\left(d_1^{(n)}-\frac{g}{\omega^2}\right)\left(\left(R_2^{(n)}\right)^4-\left(R_1^{(n)}\right)^4\right)\end{array}\right]\end{array}\right], \quad \text{for } n=p \text{ and } j=4,i=4 \text{ or } j=5,i=5\end{cases}, \tag{B16}$$

where $f_c=\mathrm{i}^{j+1}\pi\omega^2\rho$

$$U_a=\begin{cases}\left(-D_{-1,0}^{\chi}+D_{1,0}^{\chi}\right)\frac{\left(R_2^{(n)}\right)^4-\left(R_3^{(n)}\right)^4}{4\sqrt{2}R_2^{(n)}}+\left(-E_{-1,0}^{\chi}+E_{1,0}^{\chi}\right)\frac{R_2^{(n)}\left(\left(R_2^{(n)}\right)^2-\left(R_3^{(n)}\right)^2\right)}{2\sqrt{2}}, & a=0 \\ \sum_{j=1}^{\infty}\left[\begin{array}{l}\frac{(-1)^{j+1}D_{-1,j}^{\chi}+D_{1,j}^{\chi}}{\left(k_j^{(2)}\right)^2I_1\left(k_j^{(2)}R_2^{(n)}\right)}\left[\begin{array}{l}k_j^{(2)}\left(R_2^{(n)}\right)^2I_0\left(k_j^{(2)}R_2^{(n)}\right)-2R_2^{(n)}I_1\left(k_j^{(2)}R_2^{(n)}\right) \\ -k_j^{(2)}\left(R_3^{(n)}\right)^2I_0\left(k_j^{(2)}R_3^{(n)}\right)+2R_3^{(n)}I_1\left(k_j^{(2)}R_3^{(n)}\right)\end{array}\right] \\ +\frac{(-1)^{j+1}E_{-1,j}^{\chi}+E_{1,j}^{\chi}}{\left(k_j^{(2)}\right)^2K_1\left(k_j^{(2)}R_2^{(n)}\right)}\left[\begin{array}{l}k_j^{(2)}\left(R_3^{(n)}\right)^2K_0\left(k_j^{(2)}R_3^{(n)}\right)+2R_3^{(n)}K_1\left(k_j^{(2)}R_3^{(n)}\right) \\ -k_j^{(2)}\left(R_2^{(n)}\right)^2K_0\left(k_j^{(2)}R_2^{(n)}\right)-2R_2^{(n)}K_1\left(k_j^{(2)}R_2^{(n)}\right)\end{array}\right]\end{array}\right], & a=1\end{cases}, \tag{B17}$$

$$V_a=\begin{cases}-F_{-1,0}^{\chi}+F_{1,0}^{\chi}, & a=0 \\ \sum_{j=1}^{\infty}\frac{(-1)^{j+1}F_{-1,j}^{\chi}+F_{1,j}^{\chi}}{\left(k_j^{(3)}\right)^2I_1\left(k_j^{(3)}R_3^{(n)}\right)}\left[k_j^{(3)}\left(R_3^{(n)}\right)^2I_0\left(k_j^{(3)}R_3^{(n)}\right)-2R_3^{(n)}I_1\left(k_j^{(3)}R_3^{(n)}\right)\right], & a=1\end{cases}, \tag{B18}$$

$$W_a=\begin{cases}\left[\begin{array}{l}\frac{B_{-1,0}^{\chi}-B_{1,0}^{\chi}}{\left(k_0^{(1)}\right)^2J_1\left(k_0^{(1)}R_2^{(n)}\right)}\left[\begin{array}{l}k_0^{(1)}\left(R_2^{(n)}\right)^2J_0\left(k_0^{(1)}R_2^{(n)}\right)-2R_2^{(n)}J_1\left(k_0^{(1)}R_2^{(n)}\right) \\ -k_0^{(1)}\left(R_1^{(n)}\right)^2J_0\left(k_0^{(1)}R_1^{(n)}\right)+2R_1^{(n)}J_1\left(k_0^{(1)}R_1^{(n)}\right)\end{array}\right] \\ +\frac{C_{-1,0}^{\chi}-C_{1,0}^{\chi}}{\left(k_0^{(1)}\right)^2H_1\left(k_0^{(1)}R_2^{(n)}\right)}\left[\begin{array}{l}k_0^{(1)}\left(R_2^{(n)}\right)^2H_0\left(k_0^{(1)}R_2^{(n)}\right)-2R_2^{(n)}H_1\left(k_0^{(1)}R_2^{(n)}\right) \\ -k_0^{(1)}\left(R_1^{(n)}\right)^2H_0\left(k_0^{(1)}R_1^{(n)}\right)+2R_1^{(n)}H_1\left(k_0^{(1)}R_1^{(n)}\right)\end{array}\right]\end{array}\right], & a=0 \\ \sum_{j=1}^{\infty}\left[\begin{array}{l}\frac{(-1)^{j+1}B_{-1,j}^{\chi}+B_{1,j}^{\chi}}{\left(k_j^{(1)}\right)^2I_1\left(k_j^{(1)}R_2^{(n)}\right)}\left[\begin{array}{l}k_j^{(1)}\left(R_2^{(n)}\right)^2I_0\left(k_j^{(1)}R_2^{(n)}\right)-2R_2^{(n)}I_1\left(k_j^{(1)}R_2^{(n)}\right) \\ -k_j^{(1)}\left(R_1^{(n)}\right)^2I_0\left(k_j^{(1)}R_1^{(n)}\right)+2a_1^nI_1\left(k_j^{(1)}R_1^{(n)}\right)\end{array}\right] \\ +\frac{(-1)^{j+1}C_{-1,j}^{\chi}+C_{1,j}^{\chi}}{\left(k_j^{(1)}\right)^2K_1\left(k_j^{(1)}R_2^{(n)}\right)}\left[\begin{array}{l}k_j^{(1)}\left(R_1^{(n)}\right)^2K_0\left(k_j^{(1)}R_1^{(n)}\right)+2R_1^{(n)}K_1\left(k_j^{(1)}R_1^{(n)}\right) \\ -k_j^{(1)}\left(R_2^{(n)}\right)^2K_0\left(k_j^{(1)}R_2^{(n)}\right)-2R_2^{(n)}K_1\left(k_j^{(1)}R_2^{(n)}\right)\end{array}\right]\end{array}\right], & a=1\end{cases}. \tag{B19}$$

C. Displacement constraint matrix

$$
\boldsymbol{A_J} = \begin{bmatrix}
1 & 0 & 0 & 0 & 0 & -L\cos\frac{\pi}{6} & -1 & 0 & 0 & 0 & 0 & -L\sin\frac{\pi}{3} & 0 & 0 & 0 & 0 & 0 & 0 & 0 & 0 & 0 & 0 & 0 & 0 \\
0 & 1 & 0 & 0 & 0 & L\sin\frac{\pi}{6} & 0 & -1 & 0 & 0 & 0 & -L\cos\frac{\pi}{3} & 0 & 0 & 0 & 0 & 0 & 0 & 0 & 0 & 0 & 0 & 0 & 0 \\
0 & 0 & 1 & L\sin\frac{\pi}{3} & -L\cos\frac{\pi}{3} & 0 & 0 & 0 & -1 & L\cos\frac{\pi}{6} & L\sin\frac{\pi}{6} & 0 & 0 & 0 & 0 & 0 & 0 & 0 & 0 & 0 & 0 & 0 & 0 & 0 \\
0 & 0 & 0 & 1 & 0 & 0 & 0 & 0 & 0 & -1 & 0 & 0 & 0 & 0 & 0 & 0 & 0 & 0 & 0 & 0 & 0 & 0 & 0 & 0 \\
0 & 0 & 0 & 0 & 1 & 0 & 0 & 0 & 0 & 0 & -1 & 0 & 0 & 0 & 0 & 0 & 0 & 0 & 0 & 0 & 0 & 0 & 0 & 0 \\
0 & 0 & 0 & 0 & 0 & 1 & 0 & 0 & 0 & 0 & 0 & 0 & 0 & 0 & 0 & 0 & 0 & 0 & 0 & 0 & 0 & 0 & 0 & 0 \\
1 & 0 & 0 & 0 & 0 & -L\cos\frac{\pi}{6} & 0 & 0 & 0 & 0 & 0 & 0 & -1 & 0 & 0 & 0 & 0 & 0 & 0 & 0 & 0 & 0 & 0 & 0 \\
0 & 1 & 0 & 0 & 0 & L\sin\frac{\pi}{6} & 0 & 0 & 0 & 0 & 0 & 0 & 0 & -1 & 0 & 0 & 0 & L & 0 & 0 & 0 & 0 & 0 & 0 \\
0 & 0 & 1 & L\sin\frac{\pi}{3} & -L\cos\frac{\pi}{3} & 0 & 0 & 0 & 0 & 0 & 0 & 0 & 0 & 0 & -1 & 0 & -L & 0 & 0 & 0 & 0 & 0 & 0 & 0 \\
0 & 0 & 0 & 1 & 0 & 0 & 0 & 0 & 0 & 0 & 0 & 0 & 0 & 0 & 0 & -1 & 0 & 0 & 0 & 0 & 0 & 0 & 0 & 0 \\
0 & 0 & 0 & 0 & 1 & 0 & 0 & 0 & 0 & 0 & 0 & 0 & 0 & 0 & 0 & 0 & -1 & 0 & 0 & 0 & 0 & 0 & 0 & 0 \\
0 & 0 & 0 & 0 & 0 & 1 & 0 & 0 & 0 & 0 & 0 & 0 & 0 & 0 & 0 & 0 & 0 & -1 & 0 & 0 & 0 & 0 & 0 & 0 \\
1 & 0 & 0 & 0 & 0 & -L\cos\frac{\pi}{6} & 0 & 0 & 0 & 0 & 0 & 0 & 0 & 0 & 0 & 0 & 0 & 0 & -1 & 0 & 0 & 0 & 0 & 0 \\
0 & 1 & 0 & 0 & 0 & L\sin\frac{\pi}{6} & 0 & 0 & 0 & 0 & 0 & 0 & 0 & 0 & 0 & 0 & 0 & 0 & 0 & -1 & 0 & 0 & 0 & 0 \\
0 & 0 & 1 & L\sin\frac{\pi}{3} & -L\cos\frac{\pi}{3} & 0 & 0 & 0 & 0 & 0 & 0 & 0 & 0 & 0 & 0 & 0 & 0 & 0 & 0 & 0 & -1 & 0 & 0 & 0 \\
0 & 0 & 0 & 1 & 0 & 0 & 0 & 0 & 0 & 0 & 0 & 0 & 0 & 0 & 0 & 0 & 0 & 0 & 0 & 0 & 0 & -1 & 0 & 0 \\
0 & 0 & 0 & 0 & 1 & 0 & 0 & 0 & 0 & 0 & 0 & 0 & 0 & 0 & 0 & 0 & 0 & 0 & 0 & 0 & 0 & 0 & -1 & 0 \\
0 & 0 & 0 & 0 & 0 & 1 & 0 & 0 & 0 & 0 & 0 & 0 & 0 & 0 & 0 & 0 & 0 & 0 & 0 & 0 & 0 & 0 & 0 & -1
\end{bmatrix}
$$

where $L = \frac{50}{\sqrt{3}}$ m is the distance between the centre of the platform and the centre of the column in the Oxy plane.

Reference

[1] UK Department of Energy & Climate Change, *UK Renewable Energy Roadmap* (UK Department of Energy & Climate Change, 2011).

[2] UK Department for Business, Energy & Industrial Strategy, *Electricity generation costs* (UK Department for Business, Energy & Industrial Strategy, 2022).

[3] L. Hong and B. Möller, "Offshore wind energy potential in china: Under technical, spatial and economic constraints," Energy **36**, 4482–4491 (2011).

[4] D. Roddier, C. Cermelli, A. Aubault, and A. Weinstein, "Windfloat: A floating foundation for offshore wind turbines," Journal of Renewable and Sustainable Energy **2**, 033104 (2010).

[5] Y. Liu, S. Li, Q. Yi, and D. Chen, "Developments in semi-submersible floating foundations supporting wind turbines: A comprehensive review," Renewable and Sustainable Energy Reviews **60**, 433–449 (2016).

[6] A. Robertson, J. Jonkman, F. Vorpahl, W. Popko, J. Qvist, L. Froyd, X. Chen, J. Azcona, E. Uzungoglu, C. Guedes Soares, C. Luan, H. Yutong, F. Pengcheng, A. Yde, T. Larsen, J. Nichols, R. Buils, L. Lei, T. Anders Nygard, and et al., "Offshore code comparison collaboration, continuation within iea wind task 30: Phase ii results regarding a floating semisubmersible wind system: Preprint," Tech. Rep. (National Renewable Energy Lab.(NREL), 2014).

[7] J. Hu, B. Zhou, C. Vogel, P. Liu, R. Willden, K. Sun, J. Zang, J. Geng, P. Jin, L. Cui, B. Jiang, and M. Collu, "Optimal design and performance analysis of a hybrid system combing a floating wind platform and wave energy converters," Applied Energy **269**, 114998 (2020).

[8] A. Robertson, J. Jonkman, M. Masciola, H. Song, A. Goupee, A. Coulling, and C. Luan, "Definition of the semisubmersible floating system for phase ii of oc4," Tech. Rep. (National Renewable Energy Lab.(NREL), Golden, CO (United States), 2014).

[9] A. J. Coulling, A. J. Goupee, A. N. Robertson, J. M. Jonkman, and H. J. Dagher, "Validation of a fast semi-submersible floating wind turbine numerical model with deepcwind test data," Journal of Renewable and Sustainable Energy **5**, 023116 (2013).

[10] T. T. Tran and D.-H. Kim, "Fully coupled aero-hydrodynamic analysis of a semi-submersible fowt using a dynamic fluid body interaction approach," Renewable Energy **92**, 244–261 (2016).

[11] H. R. Ghafari, H. Ghassemi, and G. He, "Numerical study of the wavestar wave energy converter with multi-point-absorber around deepcwind semisubmersible floating platform," Ocean Engineering **232**, 109177 (2021).

[12] H. R. Ghafari, H. Ghassemi, and A. Neisi, "Power matrix and dynamic response of the hybrid wavestar-deepcwind platform under different diameters and regular wave conditions," Ocean Engineering **247**, 110734 (2022).

[13] L. Zhang, W. Shi, M. Karimirad, C. Michailides, and Z. Jiang, "Second-order hydrodynamic effects on the response of three semisubmersible floating offshore wind turbines," Ocean Engineering **207**, 107371 (2020).

[14] T. T. Tran and D.-H. Kim, "The coupled dynamic response computation for a semi-submersible platform of floating offshore wind turbine," Journal of Wind Engineering and Industrial Aerodynamics **147**, 104–119 (2015).

[15] M. Masciola, A. Robertson, J. Jonkman, A. Coulling, and A. Goupee, "Assessment of the importance of mooring dynamics on the global response of the deepcwind floating semisubmersible offshore wind turbine," in *The Twenty-third International Offshore and Polar Engineering Conference* (OnePetro, 2013).

[16] J. Kim and H. Shin, "Model test & numerical simulation of oc4 semi-submersible type floating offshore wind turbine," in *The 26th International*

Ocean and Polar Engineering Conference (OnePetro, 2016).

[17] L. Li, Y. Gao, Z. Hu, Z. Yuan, S. Day, and H. Li, "Model test research of a semisubmersible floating wind turbine with an improved deficient thrust force correction approach," Renewable Energy **119**, 95–105 (2018).

[18] T. Ishihara and S. Zhang, "Prediction of dynamic response of semi-submersible floating offshore wind turbine using augmented morison's equation with frequency dependent hydrodynamic coefficients," Renewable Energy **131**, 1186–1207 (2019).

[19] L. Wang, A. Robertson, J. Jonkman, Y.-H. Yu, A. Koop, A. B. Nadal, H. Li, E. Bachynski-Polić, R. Pinguet, and W. Shi, "Oc6 phase ib: Validation of the cfd predictions of difference-frequency wave excitation on a fowt semisubmersible," Ocean Engineering **241**, 110026 (2021).

[20] S. Zheng, C. Li, P. Wang, S. Zhou, and Y. Xiao, "Wind tunnel and wave flume testing on directionality dynamic responses of a 10 mw y-shaped semi-submersible wind turbine," Journal of Renewable and Sustainable Energy **15**, 013305 (2023), https://doi.org/10.1063/5.0131279.

[21] *Model Tests for Three Floating Wind Turbine Concepts*, OTC Offshore Technology Conference, Vol. All Days (2012) oTC-23470-MS, https://onepetro.org/OTCONF/proceedings-pdf/12OTC/All-12OTC/OTC-23470-MS/1605572/otc-23470-ms.pdf.

[22] H. L. Sadraddin and X. Shao, "State-of-the-art of experimental methods for floating wind turbines," Journal of Renewable and Sustainable Energy **14**, 032701 (2022), https://doi.org/10.1063/5.0071943.

[23] P. Siddorn and R. Eatock Taylor, "Diffraction and independent radiation by an array of floating cylinders," Ocean Engineering **35**, 1289–1303 (2008).

[24] R. W. Yeung, "Added mass and damping of a vertical cylinder in finite-depth waters," Applied Ocean Research **3**, 119–133 (1981).

[25] B. Child and V. Venugopal, "Optimal configurations of wave energy device arrays," Ocean Engineering **37**, 1402–1417 (2010).

[26] S. Zheng and Y. Zhang, "Wave diffraction from a truncated cylinder in front of a vertical wall," Ocean Engineering **104**, 329–343 (2015).

[27] S. Zheng and Y. Zhang, "Wave radiation from a truncated cylinder in front of a vertical wall," Ocean Engineering **111**, 602–614 (2016).

[28] A. Li and Y. Liu, "New analytical solutions to water wave diffraction by vertical truncated cylinders," International Journal of Naval Architecture and Ocean Engineering **11**, 952–969 (2019).

[29] A. Li and Y. Liu, "New analytical solutions to water wave radiation by vertical truncated cylinders through multi-term galerkin method," International Journal of Naval Architecture and Ocean Engineering **54**, 429–450 (2019).

[30] S. Zheng, A. Antonini, Y. Zhang, D. Greaves, J. Miles, and G. Iglesias, "Wave power extraction from multiple oscillating water columns along a straight coast," Journal of Fluid Mechanics **878**, 445–480 (2019).

[31] S. Zheng, Y. Zhang, J. Liu, and G. Iglesias, "Wave diffraction from multiple truncated cylinders of arbitrary cross sections," Applied Mathematical Modelling **77**, 1425–1445 (2020).

[32] D. Ning, Y. Zhou, and C. Zhang, "Hydrodynamic modeling of a novel dual-chamber owc wave energy converter," Applied Ocean Research **78**, 180–191 (2018).

[33] S. Michele, E. Renzi, C. Perez-Collazo, D. Greaves, and G. Iglesias, "Power extraction in regular and random waves from an owc in hybrid wind-wave energy systems," Ocean Engineering **191**, 106519 (2019).

[34] P. Cong, Y. Liu, Y. Gou, and B. Teng, "Theoretical modeling of hydrodynamic characteristics of a compound column-plate structure based on a novel derivation of mean drift force formulation," Proceedings of the Institution of Mechanical Engineers **233**, 1022–1036 (2018).

[35] C. M. Chiang, M. Stiassnie, and D. K.-P. Yue, *Theory and Applications of Ocean Surface Waves* (World Scientific, 2005) https://www.worldscientific.com/doi/pdf/10.1142/5566.

[36] Y. Li, X. Zhao, Q. Zou, and J. Geng, "Hydrodynamic performance of dual-chamber oscillating water column array under oblique waves," Physics of Fluids **34**, 117112 (2022), https://doi.org/10.1063/5.0118655.

[37] S. Zheng, M. H. Meylan, D. Greaves, and G. Iglesias, "Water-wave interaction with submerged porous elastic disks," Physics of Fluids **32**, 047106 (2020), https://doi.org/10.1063/5.0006119.

[38] C. Wang, S. Zheng, and Y. Zhang, "A heaving system with two separated oscillating water column units for wave energy conversion," Physics of Fluids **34**, 047103 (2022), https://doi.org/10.1063/5.0086581.

[39] A.-j. Li and Y. Liu, "Hydrodynamic performance and energy absorption of multiple spherical absorbers along a straight coast," Physics of Fluids **34**, 117102 (2022), https://doi.org/10.1063/5.0118052.

[40] R. Antonutti, C. Peyrard, L. Johanning, A. Incecik, and D. Ingram, "The effects of wind-induced inclination on the dynamics of semi-submersible floating wind turbines in the time domain," Renewable Energy **88**, 83–94 (2016).

[41] M. Philippe, A. Babarit, and P. Ferrant, "Aero-hydro-elastic simulation of a semi-submersible floating wind turbine," Journal of Offshore Mechanics and Arctic Engineering **136** (2014), https://doi.org/10.1115/1.4025031.

[42] S. Zheng and Y. Zhang, "Theoretical modelling of a new hybrid wave energy converter in regular waves," Renewable Energy **128**, 125–141 (2018).

[43] A.-J. Li, H. Fang, and Y. Liu, "Hydroelastic analysis of interaction between water waves and a floating laminated disk," Physics of Fluids **34**, 047121 (2022), https://doi.org/10.1063/5.0088675.

[44] F. Cao, M. Han, H. Shi, M. Li, and Z. Liu, "Comparative study on metaheuristic algorithms for optimising wave energy converters," Ocean Engineering **247**, 110461 (2022).

[45] K. Zhu, H. Shi, M. Han, and F. Cao, "Layout study of wave energy converter arrays by an artificial neural network and adaptive genetic algorithm," Ocean Engineering **260**, 112072 (2022).

[46] J. Gao, X. Ma, G. Dong, H. Chen, Q. Liu, and J. Zang, "Investigation on the effects of bragg reflection on harbor oscillations," Coastal Engineering **170**, 103977 (2021).

[47] D. Ning, S. Zhang, L. Chen, H.-W. Liu, and B. Teng, "Nonlinear bragg scattering of surface waves over a two-dimensional periodic structure," Journal of Fluid Mechanics **946**, A25 (2022).

[48] J. Peng, A. Tao, Y. Liu, J. Zheng, J. Zhang, and R. Wang, "A laboratory study of class iii bragg resonance of gravity surface waves by periodic beds," Physics of Fluids **31**, 067110 (2019), https://doi.org/10.1063/1.5083790.

[49] Y. LI and C. C. MEI, "Bragg scattering by a line array of small cylinders in a waveguide. part 1. linear aspects," Journal of Fluid Mechanics **583**, 161–187 (2007).

[50] X. Garnaud and C. C. Mei, "Bragg scattering and wave-power extraction by an array of small buoys," Proceedings of the Royal Society A: Mathematical, Physical and Engineering Sciences **466**, 79–106 (2010), https://royalsocietypublishing.org/doi/pdf/10.1098/rspa.2009.0458.

[51] C. M. LINTON, "Water waves over arrays of horizontal cylinders: band gaps and bragg resonance," Journal of Fluid Mechanics **670**, 504–526 (2011).

[52] X. Zhao, R. Xue, J. Geng, and M. Göteman, "Analytical investigation on the hydrodynamic performance of a multi-pontoon breakwater-wec system," Ocean Engineering **220**, 108394 (2021).